

EVLA Memo 212

VLA Holography

Rick Perley

July 21, 2021

Abstract

I describe the implementation and results of the VLA holography program. The initial, major round of panel adjustments was completed in 2000, providing at least a doubling in high frequency sensitivity. Following the completion of the EVLA project, a secondary round of adjustments was started in 2011, and is ongoing. Most VLA antennas have a surface rms of 0.35 mm or better. Further adjustments, using data already in hand, can reduce this to typically 0.25 mm, and possibly as low as 0.15 mm – adequate for the VLA’s highest operating frequency of 50 GHz. The surfaces remain very stable over many years, so that further observations and adjustments are not likely to be necessary, barring some catastrophic event.

1 Introduction

The VLA antennas were designed for a maximum operating frequency of 23 GHz. With the implementation of the Q-band (40 – 50 GHz) receiver system in the early 1990s, and the addition of the Ka-band (28 – 40 GHz) system as part of the VLA Expansion Project, a significant improvement in VLA antenna capabilities at high frequencies was required. Improvements in antenna pointing, antenna optical alignment, and antenna efficiency have been made. The major pointing improvements came with the implementation of referenced pointing in the early 1990s, and which provides, in best-weather conditions, pointing accuracies of ~ 4 arcseconds, sufficient for the ~ 60 arcsecond beam of the Q-band system. Improvements in the antenna optics (specifically, in the alignment of the subreflector and the refinement of the ‘subreflector rotation trick’) are now completed, and are described in EVLA Memo 211.

The VLA holography program began in 1992, with the first useable data taken in July of that year. The holography procedures were developed by Mike Kesteven during his year-long visit to the VLA in 1993, and remain in use today. The initial results of the early holography program, on VLA antenna #4, are reported in VLA Test Memo #173, September 1993. The panel adjustment procedures are described in Bob Broilo’s VLA Test Memo #174. A good review of the development of antenna holography, showcasing the early results from VLA holography, is found in Mike’s 1994 paper ‘Microwave Holography for Antenna Metrology’, IE Aust. & IREE Aust. **14**, 85, 1994. The initial round of panel adjustments was completed in 2000. Following the implementation of new wide-band receivers and correlator by the EVLA Project, the antennas have been re-surveyed and further adjustments are ongoing.

In this memo, I describe in some detail the long-running efforts to improve the accuracy of the VLA primary reflector shape through antenna holography.

2 Basics

2.1 Principles of Holography

Antenna holography makes use of the Fourier transform relationship between the complex electric field over a radiating aperture, $E(u, v)$, and the antenna’s far-field electric field distribution $P(l, m)$ ¹:

$$P(l, m) = \int_{-\infty}^{\infty} \int_{-\infty}^{\infty} E(u, v) e^{-i2\pi(lu+mv)} dudv \quad (1)$$

In this expression, $u = x/\lambda$ and $v = y/\lambda$ are rectilinear coordinates, in wavelengths, in the antenna aperture plane. We utilize a right-handed system, looking into the antenna aperture, so that positive u describes a position to the right

¹According to Bracewell, this relationship is only strictly valid for small angles away from the pointing direction. This condition is easily met for high-gain antennas, such as we are considering here.

side of the antenna, and positive v describe a position above the center. The direction cosines in the horizontal and vertical directions, l, m , are defined with respect to this aperture plane. In contrast to the aperture plane definitions, we define the direction cosines from an outward looking perspective: Positive l and m labels that quadrant of the antenna's radiation pattern to the right and above the center of the beam.

Given knowledge of the far-field complex (amplitude and phase) beam pattern, an inverse Fourier transform of equation (1)

$$E(u, v) = \int_{-1}^1 \int_{-1}^1 P(l, m) e^{i2\pi(lu+mv)} dl dm \quad (2)$$

generates an image of the (complex) E-field voltages in the radiating aperture. This image is not directly that which describes the electric field at the surface of the antenna, but is instead the field over an imaginary planar surface, perpendicular to the direction of the main beam. We refer to this plane in this memo as the 'Effective Radiating Aperture' – often denoted by 'ERA'. It is convenient to select the plane passing through the parabolic antenna focus, although there is no special benefit in doing so.

Measuring the far-field beam pattern $P(l, m)$ is a relatively easy task for an interferometer array. One or more of the array elements – the 'reference antennas' – track a suitably strong and distant point source. The remaining elements – the 'target antennas' – scan this same object over a finite range of angles. The source of emission must be much smaller than the antenna beamwidth, (and preferably unresolved), and in the far-field of the antenna². The complex correlation products between target and reference antennas provide voltages proportional to the primary beam voltage patterns. Note that although the output correlation is the product of two signals – and hence has units of power – the values are in fact proportional to the voltage pattern of the target antennas, since the reference antenna responses are constant. The target antennas can either scan the beam continuously, or step through a raster pattern, with stepsizes Δl and Δm , and with $\Delta\tau$ seconds of integration on each point³. These data products can be calibrated using standard methods developed for interferometric astronomical observing.

In the following, it is assumed that the two voltages provided by the antenna, labelled 'R' and 'L', are uniquely related to the actual RCP and LCP components of the electric fields. In fact, this is not strictly true, as antenna cross-polarization 'leaks' a small part of LCP into the 'R' output, and vice versa. However, the effect of the contamination is small – typically only 1% in the parallel-hand correlations if the target source is unpolarized – and is neglected in the following analysis⁴.

The VLA on-line software uses the discrete step method, with astronomical calibrators as emission sources. There are two major advantages of using astronomical sources, rather than an artificial beacon, for the emission source: (i) Near-field corrections are not necessary, and (ii) the observations can be done at many bands or frequencies, at any elevation, and with the antennas at any location. The major disadvantage of an astronomical source is that sensitivity may be limited, especially at higher frequencies where receiver sensitivity is poorer. However, for the VLA's high-gain antennas and wide-band receivers, sensitivity is usually not a limiting issue, as explained in Section 2.2.3.

Because the observations are discretely sampled, the integral relationship given in eqn. (2) must be replaced with its discrete analog. If $S(l, m)$ is the sampling function describing the locations in l, m space where the samples are located, eqn. (2) becomes

$$E_m(u, v) = \int_{-1}^1 \int_{-1}^1 S(l, m) P(l, m) e^{i2\pi(lu+mv)} dl dm \quad (3)$$

where the calculated illumination $E_m(u, v)$ will differ from the true, due to the effects of the sampling: $E_m(u, v) = E(u, v) * B(u, v)$, where $B(u, v)$ is the Fourier transform of the sampling function, and $(*)$ represents the convolution operation. Since $S(u, v)$ is always known, the smoothing effects of the limited sampling can always be estimated.

If the sampling is done on a regular grid, it can be represented by

$$S(l, m) = {}^2\text{III}(l, m) \square(l/L) \square(m/M) \quad (4)$$

where $\square(l/L)$ and $\square(m/M)$ are the (centered) rectangle functions of full width L and M , and ${}^2\text{III}(l, m)$ is Bracewell's

²Near-field observations are certainly possible, and are commonly used at other telescopes, but require correction for the curvature of the incoming wavefront.

³Other patterns can be imagined, and are being used at other arrays – radial cuts, and spirals centered at the beam center for example. However, these are less efficient than a regular grid, which optimally samples the beam pattern.

⁴Note that this is the cross-coupling due to electronics, multiple scattering, etc. The separation of the R and L beams due to beam squint is considered a spatially-variant gain effect.

two-dimensional ‘bed-of-nails’ function,

$${}^2\text{III}(l, m) = \sum_{j=-\infty}^{\infty} \sum_{k=-\infty}^{\infty} {}^2\delta(l - j\Delta l, m - k\Delta m) \quad (5)$$

and where Δl and Δm are the stepsizes in the two coordinate directions. The transform relationship then becomes

$$E_m(u, v) = \sum_{j=-J}^J \sum_{k=-K}^K e^{i2\pi(j\Delta l u + k\Delta m v)} P(j\Delta l, k\Delta m) \quad (6)$$

where $J = L/(2\Delta l)$, and $K = M/(2\Delta m)$ are the number of samples on each side of the beam center.

The discrete transform given above provides us with an image of the ‘Effective Radiating Aperture’. This will differ from the true distribution of electric field over the antenna surface, due to a number of important effects, listed below.

- **Limitations in beam sampling** The sampling will be limited in maximum angle, may be non-uniform, and may be missing points. The effect of maximum angle is straightforward to estimate: it leads to a convolution of the true radiating aperture image with an effective beam. For our case with regular sampling and with maximum offset angles $L/2$ and $M/2$, the smoothing function is given by

$$B(u, v) = \text{sinc}(Lu)\text{sinc}(Mv) \quad (7)$$

The FWHM of this function is given, in physical units, by $W = 1.27\lambda/L$. A typical raster for VLA holography has a full extent $L \sim 43\lambda/D$, leading to a physical resolution of about 80 cm, about half the size of a typical panel.

Non-uniformities in beam sampling are more difficult to deal with, as they cause over- or under-weighting of portions of the measurement plane, leading to a mis-representation of the ERA if the straight summation implied by equation (3) is done. If the antenna beam has been significantly oversampled in general, the situation could be handled in the same way as for astronomical imaging – by gridding and regularly re-sampling the data, followed by the transform. However, for the VLA, time duration arguments dictate sampling close to the critical sampling increment. For near-critical sampling, use of gridding and resampling will not be effective. Far better is to establish a regularly sampled grid at the time of measurement, followed by a direct (i.e., not gridded) Fourier sum. This has been implemented, as described below in Section 2.2.1.

- **Optics Errors** Misalignments of the antenna’s feed or subreflector impose large-scale phase gradients across the aperture. These must be measured and removed before the phase in the ERA can be related to antenna surface errors. We utilize a simple model by Ruze (1969) for these corrections, as described below in section 2.2.2.
- **Geometric Corrections for the Panel Phase** The resulting phase from the transform is that of the ‘equivalent radiating aperture’. If the deviations in this from zero phase are due to panel displacements, a geometric correction factor is required, as described in Section 2.2.5.

2.2 The Devil is in the Details

In this section, we provide details on the issues raised above.

2.2.1 Antenna Rasters

The adopted procedure is to scan the target antennas across a strong source, using one or more fixed reference antennas, then Fourier transform the measured complex visibility function. Conversion from the beam measurements to the antenna aperture plane is simplest if the raster data are taken on a rectilinear grid in the (l, m) coordinates. Enabling a uniform sampling grid in the direction cosines avoids issues of gridding and weighting, and enables a straightforward ‘Direct’ transform.

The VLA’s antennas are azimuth-elevation, so we need to derive the relationship between the target source position (A_s, E_s) and the antenna’s pointing direction (A_a, E_a) for a desired offset in the antenna direction cosines (l, m) . The relationships are⁵:

$$l = \sin \alpha = \cos E_s \sin(A_s - A_a) \quad (8)$$

$$m = \sin \beta = \sin E_s \cos E_a - \cos E_s \sin E_a \cos(A_s - A_a). \quad (9)$$

⁵Here we use the VLA’s definition of azimuth: positive for a clockwise rotation from north, viewed from above

Note that in the special case of small azimuth offsets ($A_s - A_a \ll 1$), and small elevation offsets ($E_s - E_a \ll 1$), these equations become: $l = \cos E_s (A_s - A_a)$, and $m = E_s - E_a$. The angles α and β are the angular offsets, relative to the beam center, along the l and m axes.

Inversion of equations (8) and (9) gives the antenna antenna pointing position (A_a, E_a) in terms of the source position (A_s, E_s) and the desired (l, m) coordinates:

$$A_a = A_s - \arcsin(l \sec E_s) \quad (10)$$

$$\sin E_a = \frac{\sin E_s \sqrt{1 - l^2 - m^2} - m \sqrt{\cos^2 E_s - l^2}}{1 - l^2} \quad (11)$$

For small azimuth and elevation offsets, these equations simplify to

$$A_a = A_s - l \sec E_s \quad (12)$$

$$E_a = E_s - m. \quad (13)$$

which are usually sufficient for high-frequency dish holography.

These definitions ensure that pointing the antenna to a smaller azimuth than the target source will sample regions of positive l , while pointing to a lower elevation samples regions of positive m ⁶, consistent with our definition of these angles. Low-frequency wide-angle L-band holography (to be described in a subsequent memo) has allowed direct confirmation of these conventions by initiating a holography observation with a large (17 degree) offset for the initial position, and observing which direction the antenna moved to reach the desired start point.

Critical sampling requires a grid spacing no larger than $\Delta l = \Delta m = \lambda/D$ for a circular antenna of diameter D . A minimum panel resolution of $\sim 1\text{m}$ suggests maximum offsets of at least $\sim 15\lambda/D$. For high frequency holography, this maximum offset is very small – about 15 arcminutes at 43 GHz, so the offset angles could be set by steps constant in both azimuth and elevation, utilizing equations 12 and 13. However, at 1400 MHz, this maximum offset angle will exceed 7 degrees (and is near 35 degrees at 327 MHz!), where the curvature in the sampling pattern by using a constant step increment becomes very large. This point is shown in Figure 1, showing the sampling pattern for an L-band holography observation taken at an elevation of 72 degrees and maximum offset of 0.21 radians (= 12 degrees). On the left is the desired sampling pattern, on the right is what is obtained when using a constant stepsize of 0.01 radians in elevation, and 0.01 $\sec E_s$ radians in azimuth⁷. Utilization of a constant stepsize in the sampling for az-el antennas can lead to very non-uniform sampling of the antenna beam. In general, for holography at low frequencies, or at high elevations, utilization of the proper equations (10 and 11) is essential.

The current version of the ‘Executer’ holography raster program, written by Michiel Brentjens in 2011, has implemented square grid sampling, and is valid for all offsets and elevations up to 87 degrees. Due to the potentially excessive azimuth travel time for raster positions at high elevation, an (l, m) pointing request requiring an antenna elevation above 87 degrees is deferred until the end of the observation, with the expectation that the source will be at a lower elevation by that time. If still not possible, that pointing is skipped. Furthermore, pointings within a raster line for which the slew (movement) time is longer than a third of the requested dwell time will also be deferred to the end. Readers wishing a more thorough description should refer to Michiel’s documentation.

2.2.2 Removing Optics Alignment Errors

Optical alignment errors of the feed or subreflector, and pointing offsets of the main reflector, will introduce significant large-scale phase errors across the ERA which must be removed before the panel displacements can be determined. To do this, a model of the effects of small perturbations in antenna subreflector and feed locations is required. We have implemented the model due to Ruze (1969). A full description of the model is given in the Appendix of EVLA Memo #211. Here I briefly summarize the results.

If the subreflector is vertically displaced (i.e., a focus error) by an amount Δz , the path length from the ERA at position (r, ϕ) to the Cassegrain focus is changed by

$$\Delta d(r) = \Delta z \left(\frac{1 - Q^2}{1 + Q^2} + \frac{1 - q^2}{1 + q^2} \right) \quad (14)$$

where $q = r/2f$, $Q = r/2Mf$, r is the radial offset of the point in question, f is the focal length (8.8 meters for the VLA), and M is the magnification (13 for the VLA). The error pattern created by a focus change comprises even powers

⁶Pointing above the source can sample positive values of m if the azimuth offset is sufficiently large – this occurs when $\cos(\delta A) < \tan(E_s)/\tan(E_a)$.

⁷This would correspond to 1440 MHz for our standard sampling step of $1.2\lambda/D$

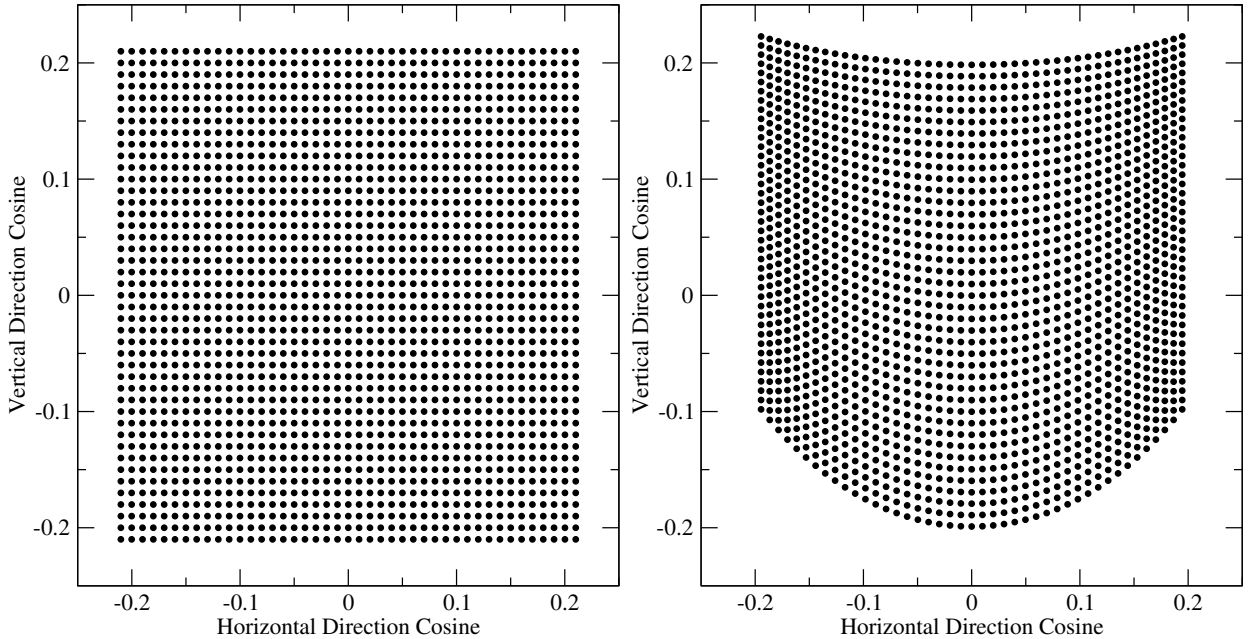


Figure 1: The left panel shows the desired angular sampling for a 43 x 43 grid, with spacing 0.01 radians – appropriate for L-band on the VLA. The right panel shows the actual sampled area for $E_s = 72$, when observed at meridian transit, if a uniform stepsize of 0.01 radians in elevation, and $0.01/\cos E_s$ in azimuth is utilized.

of r , so resembles a ‘bull’s-eye’ in the ERA. Because of the assumed axisymmetric geometry, there is no dependency on the azimuth angle ϕ .

If the subreflector is offset laterally by an amount Δx , the resulting path length change from the point (r, ϕ) in the ERA plane to the Cassegrain feed becomes

$$\Delta d(r, \phi) = 2\Delta x \left(\frac{Q}{1+Q^2} - \frac{q}{1+q^2} \right) \cos \phi \quad (15)$$

The error pattern now comprises odd powers of the radius r . The dominant term is a linear phase ramp centered at the center of the ERA. The linear portion of this ramp causes an offset of the beam pointing position, while the higher-order odd terms result in a distortion of the beam shape, and loss of efficiency. The pointing offset due to a lateral subreflector shift is removed by the antenna referenced pointing calibration procedures which are embedded into the OPT holography function. The effect on the aperture plane phase is to remove a linear phase slope, so that the path length dependence becomes

$$\Delta d(r, \phi) = 2\Delta x \left(\frac{Q}{1+Q^2} - \frac{q}{1+q^2} + \kappa q \right) \cos \phi \quad (16)$$

where κ is a coefficient which is close to 0.7^8 for the VLA antennas.

Illustrations of these phase perturbations at a frequency of 30 GHz are shown in figure 2. These were generated by the AIPS task HOLOG, which implements the Ruze model to generate images of the phase perturbations due to small displacements in the feed or subreflector positions. The figure shows how small subreflector offsets cause significant large-scale phase perturbations. The left panel shows the phase distribution from a 1mm downward offset of the subreflector at 1cm wavelength, normalized to the dish center. The error pattern is even, with a 25 degree differential between the rim and the center. The center panel shows the uncompensated error pattern from a 10 mm horizontal lateral offset of the subreflector, again at 1cm wavelength. The effect is significant, with nearly two full turns of phase between opposite sides. The first-order effect of this is a ~ 2.5 arcminute offset of the beam. When this is removed (by referenced pointing), the resultant phase distribution is as shown in the right hand panel. With the overall slope removed, the effect on the beam is a distortion which shows up most sensitively in the inner sidelobes. This is a subject of EVLA Memo 211, and is discussed thoroughly there.

⁸This was determined empirically, but can also be determined from simulations based on observed data. The value depends on the illumination weighting function.

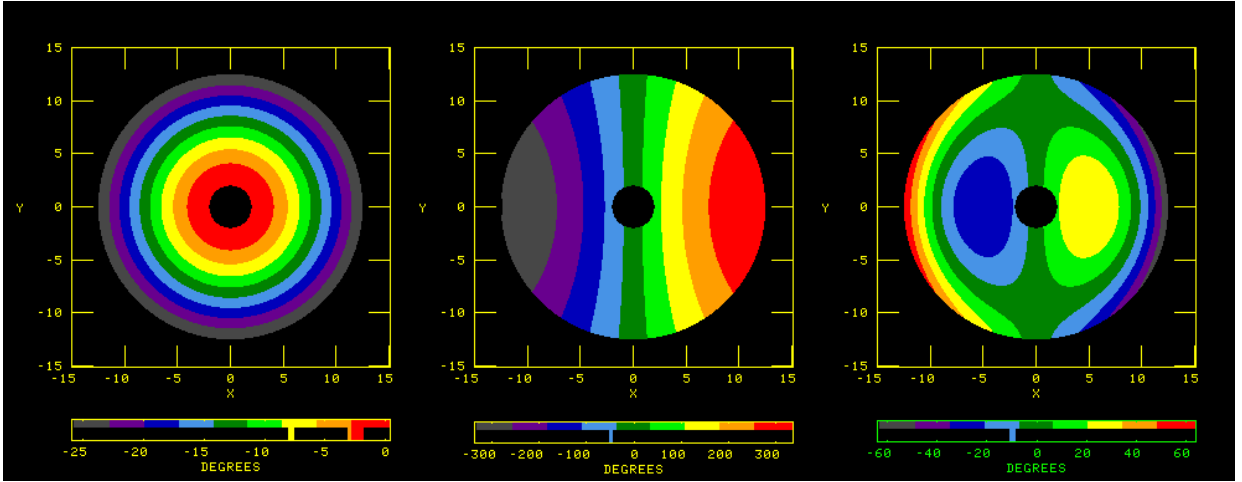


Figure 2: Showing the effects of simple optics errors due to misplacement of the subreflector. The left panel shows the phase distribution at $\lambda = 1\text{cm}$ wavelength due to a 1mm downwards offset of the focus. The middle panel shows the effects of a 1cm lateral offset without repointing, and the right panel shows the phase perturbations after the pointing error associated with the offset is removed.

To prevent these large-scale optics errors from modifying the panel adjustments, it is necessary to remove them prior to calculating panel phase patterns. The AIPS task HOLOG solves for and removes these large scale perturbations, as described in Section 3.2.4.

2.2.3 Sensitivity

Real data have noise, which degrades the accuracy of the derived antenna illumination. Here I utilize a simple argument to derive the relationships.

Consider a uniformly illuminated square aperture of full width $u_{max} = D/\lambda$ and $v_{max} = D/\lambda$. The illumination function is given by

$$E(u, v) = {}^2 \Pi (u/u_{max}, v/v_{max}) = {}^2 \Pi (\lambda u/D, \lambda v/D) \quad (17)$$

The far-field beam is then given by

$$P(l, m) = \text{sinc}(Dl/\lambda)\text{sinc}(Dm/\lambda). \quad (18)$$

This is the product of two oscillatory functions, with nulls at all multiples of $\Delta l = \lambda/D$ and $\Delta m = \lambda/D$.

Now imagine sampling this beam, using critical sampling, for which $\Delta l = \Delta m = \lambda/D$. Presume a square grid of N by N , so there are N^2 individual measurements. For this square aperture beam, all samples are at the nulls, except the one at $l = 0, m = 0$, for which the (calibrated) amplitude of the measured sample is S , the spectral flux density of the observed source.

The derived aperture illumination at the origin is the sum over all measured values:

$$E_m(0, 0) = \sum_{j=-n}^n \sum_{k=-n}^n P(j\Delta l, k\Delta m) \quad (19)$$

where $n = (N - 1)/2$ is the number of measured values on each side of the origin. By construction, the same result will be obtained for any point within the square aperture.

Suppose the observations are taken on a source of spectral flux density S Janskys, using a bandwidth of B Hz, and an integration time, per point, of τ seconds. The derived illumination, for this case, will then simply be

$$E(0, 0) = S \quad (20)$$

since all sampled values, except the central one, are on the beam nulls.

The noise in this measurement is given by the square root of the summed noise values over all N^2 values. For each individual sample, the $1\text{-}\sigma$ noise, in Stokes I, is given by

$$\sigma = \frac{S_a}{2\sqrt{B\tau}}. \quad (21)$$

where S_a , the antenna's equivalent flux density, is given by

$$S_a = \frac{2kT_{sys}}{\epsilon A_p} \quad (22)$$

and ϵA_p is the effective antenna aperture. The efficiency factor ϵ comes from the illumination taper and the effect of blockage due to the subreflector, quadrupod legs, etc. For this application, it does not include the effects of lost efficiency due to the surface irregularities. For the VLA, Napier (1999) has $\epsilon = 0.85$.

Summed over all N^2 values, the noise per computed point becomes

$$\sigma = \frac{NS_a}{2\sqrt{B\tau}}. \quad (23)$$

Hence, the SNR of any of the panel measurements is

$$SNR = \frac{2S\sqrt{B\tau}}{NS_a}. \quad (24)$$

This is the SNR of the illumination amplitude. More important is the error in the illumination phase. For the high SNR situation, this is simply $\sigma_\phi = 1/SNR$, so that in terms of physical displacement

$$\sigma_{panel} = \frac{\lambda}{4\pi SNR \cos \theta} \quad (25)$$

where θ is the tilt angle of the antenna surface with respect to the horizontal, and where the relation given in eqn 35 has been used.

Although this argument is based on a uniformly illuminated square aperture, it should apply to more realistic situations, as the reduction in forward gain due to tapering or panel irregularities will be compensated by larger, and unsymmetrically positioned sidelobes. At the least, the dependencies shown in the result will be retained, while a small change in scaling factor may occur.

Receiver noise can be significant for VLA holography at high frequencies. At Q-band, with $S_a \sim 500$ Jy, $B = 100$ MHz, $N = 43$, and $\tau = 7$ seconds, a 1 Jy target source provides an SNR of only 2.4. A 10 Jy source is thus a minimum requirement for effective panel holography at this frequency.

Besides using a strong target source, there are four other – less effective – ways to improve the SNR:

- Widen the bandwidth
- Increase the integration time per point
- Oversample the grid
- Employ multiple reference antennas.

We discuss each, in turn.

- Bandwidth Averaging

The SNR equation (Eq. 24) shows SNR improving with the square root of the bandwidth. However, averaging the data over frequency degrades the large-angle measurements, as the antenna beam sidelobes expand linearly with wavelength. Hence, averaging the data over frequency will smooth out the variations which contain the information on the panel displacements we're trying to measure.

A limit on the bandwidth can be established from a simple argument, again based on a uniformly illuminated square aperture. We have shown above that the beam for such an aperture is given by

$$P(l, m) = \text{sinc}(Dl/\lambda)\text{sinc}(Dm/\lambda). \quad (26)$$

On each axis, the beam response has zeros at offset angles given by $l = n\lambda/D$. For large values of n , the beam sidelobes are approximately sinusoidal, with period $2\lambda/D$.

The sidelobe pattern expands linearly with wavelength. Hence, averaging over frequency effectively averages the sidelobe response pattern over radius, thus degrading the amplitude. Figure 3 illustrates the problem. Here are plotted the beam amplitudes as a function of offset (in normalized units of λ/D) for a uniformly weighted square aperture at two frequencies – the upper frequency is 2.5% higher than the lower. After 20 nulls, the two response

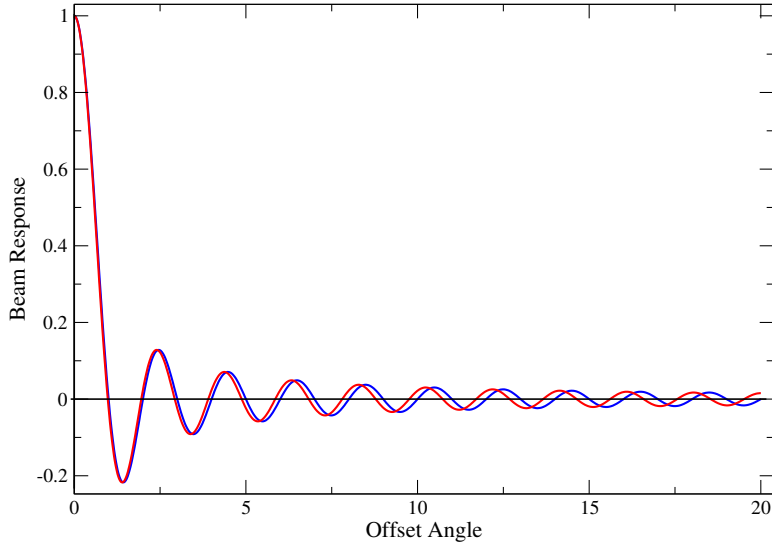


Figure 3: The beam profile as a function of offset angle for a uniformly illuminated square aperture, for two observing wavelengths with a ratio of 1.025

functions are becoming distinctly different. Averaging at a given offset will degrade the measured amplitude, leading to a blurring of the derived aperture distribution. A tolerable loss, of less than 10% at the largest offset angle, will occur if the shift of the oscillatory sidelobes due to the spread in wavelength over the spectral window is less than 1/8 of a full sidelobe cycle at the central wavelength. This occurs when

$$N_n(\lambda_l - \lambda_s) = \lambda_0/4 \quad (27)$$

where N_n is the number of nulls. In terms of central frequency, $\Delta\nu_o$ and bandwidth $\Delta\nu$, we have (presuming $\Delta\nu \ll \nu_0$)

$$\Delta\nu < \nu_0/4N_z \quad (28)$$

where N_z is the N^{th} zero in the sidelobe beam pattern at the largest angular offset. For a grid of (full-width) N points, with oversampling factor f , $N_z = (N - 1)/2f$, leading to

$$\Delta\nu < \frac{f\nu_0}{2(N - 1)} \quad (29)$$

For the VLA, we normally use $N = 43$ and $f = 1.2$. The maximum bandwidth permitted to minimize information loss at the largest offsets is then $\Delta\nu = \nu_0/70$. At X-band, this gives 114 MHz. The maximum SPW width for the VLA is 128 MHz, so we conclude that for holography at frequencies at or above 8 GHz, the full 128 MHz wide spectral window can be safely combined prior to image formation.

If the full 128 MHz width of a spectral window is insufficient to provide the desired SNR, multiple spectral windows can be individually utilized, and the results averaged.

There is another means of avoiding spectral smearing – Fourier inversion of all the channelized data without spectral averaging. The major disadvantage of this is the large increase in computational effort. Both this method, and the averaged SPW routine described above, require the illumination function to be unchanged over the desired spectral width. Comparison of results as a function of SPW indicates this is in fact the case.

- Time Averaging

This is the easiest way to increase sensitivity, but the cost in overall observing time is significant. For a standard grid of 43 x 43 points, 5.1 hours is required for 10 seconds per point – independent of calibration, which requires an additional 20% overhead. Doubling the integration time per point to 20 seconds is not a practical option unless multiple observing days are envisioned.

- Multiple Reference Antennas

The most practical way to improve SNR is to employ multiple reference antennas. For N_r reference antennas, the signal rises linearly with N_r , while the noise rises with the square root of this factor. Hence, for multiple reference

antennas, the SNR becomes

$$SNR = \frac{2S\sqrt{N_r B\tau}}{NS_a} \quad (30)$$

This is an attractive option, as two individual runs are always needed for a full-array holography. The array is split into two halves – for the first day, the first half are reference antennas, the second half are target antennas. The roles are reversed on the second day. The SNR is increased by a factor of about $\sqrt{13} \sim 3.6$ if half the elements are reference antennas, compared to a single reference antenna. Besides increasing the SNR, reference and target antennas can be alternated down the array arms, allowing bracketing of the target antennas, which minimizes atmospheric phase effects.

- Oversampling

SNR is improved by oversampling. The simplest argument to show this is to note that if the beam is oversampled by a factor of f , the signal increases by a factor of f^2 , while the noise increases by f . Hence the SNR increases by f .

Those wishing a precise calculation can note the following, which again presumes a square aperture of full width D : Write the summation over the beam in terms of an oversampling factor, f , so that the sampling interval is $\Delta l = \lambda/fD$. Then,

$$E_m(0,0) = \sum_{j=-n}^n \sum_{k=-n}^n \text{sinc}\left(\frac{j}{f}\right) \text{sinc}\left(\frac{k}{f}\right) \quad (31)$$

where n is the number of points on each side of the beam center. The sums can be executed in two steps: First, the summation over l at $m = 0$ is written:

$$S_{m=0} = 1 + \frac{2f}{\pi} \sum_{n=1}^N \frac{\sin(n\pi/f)}{N} \quad (32)$$

for critical sampling, $f = 1$, the sum on the right hand side is zero, so $S_{m=0} = 1$, as before. For $f = 2$, the sum on the right hand side goes to $\pi/2$ as $N \rightarrow \infty$. The series converges fairly rapidly (within 5% after 20 terms), so we will use this limiting value, thus $S_{m=0} = 2$. For non-zero values of m , the summation over l is the same series, multiplied by the m -intercept value of the beam function. The summation over m is then identical to that over l , giving the same result – twice the central value. Hence, the overall summation, with 2 times oversampling, is 4. Since the summed noise rises as the square root of the total number of points, the increase in SNR equals 2 – the oversampling factor. Other sampling factors will lead to summations over different series, which we expect to provide the same result – the increase in signal goes as f^2 , while the increase in noise rises as f , so $SNR \propto f$.

This is not a cost-effective way to increase sensitivity, since oversampling reduces the number of measured gridpoints per unit area. The time taken increases with f^2 in order to get an approximately linear improvement in SNR.

However, it is important some modest oversampling be included, as the regularly sampled data lead to aliasing in the transform plane. The value of $f = 1.2$ is a good compromise amongst sensitivity, time, and errors arising from aliasing.

2.2.4 Sensitivity – Comparison to Observations

The sensitivity equation, including the factors of oversampling and multiple reference antennas, is

$$SNR = \frac{2Sf\sqrt{N_r B\tau}}{NS_a} \quad (33)$$

A number of tests have been done to confirm this relation. Using high-quality observations at Ka-band taken in May 2020, illumination amplitude and panel displacement images were made with various combinations of bandwidth, number of reference antennas, and grid size. The results of these confirmed all the functional relations shown in equation 33, with the exception that the bandwidth dependence flattens beyond a bandwidth of ~ 100 MHz. This is probably a result of amplitude calibration errors – likely related to pointing variations – whose effects become visible in the illumination amplitude images due to the increased sensitivity from the use of wide bandwidths.

One significant (but helpful) discrepancy was found in these tests – the effective SEFD (S_a in equation 33) was found to be $\sim 30\%$ lower than expected from application of equation (22). This results in a sensitivity $\sim 30\%$ better than predicted! Possible origins for this discrepancy are: a calibrator flux 30% higher than assumed (no direct flux density measurement was made, but the visibility amplitudes, after correction with switched power, indicate the value of ~ 5

Jy given in the calibrator manual for J1743-0350 is correct); the system temperature is 30% lower than the value of 50K suggested by the switched power and used in equation 22; or that a factor of $\sim \sqrt{2}$ is missing from the sensitivity equation.

Tests were also performed to check for performance differences between the eight spectral windows available in May 2020 – all eight gave identical results to within the measurement noise.

2.2.5 Effect of Calibration Errors

Random atmospheric phase errors which are uncorrelated on timescales similar to the step time (normally 10 seconds) will degrade sensitivity in the same way as observing a weaker source. Atmospheric phase errors generally increase with baseline length, so if the phase stability is poor, use of close-by reference antennas will be necessary. Experience has shown that if the typical phase irregularities are less than a \sim half a radian, their effects on the results are unimportant. The number of suitable reference antennas (if more than two are thought necessary) will thus depend on the atmospheric phase stability. The decision of how many to use then depends on examination of the calibrator phase solutions.

Pointing errors are not important if they are constant over the period of the observation. (As noted before, a simple pointing error introduces a phase gradient, which is removed by software). Variable pointing errors are important if the pointing offsets approach the stepsize of the measurement grid. For a 1cm wavelength ($\nu = 30$ GHz), the stepsize is ~ 80 arcseconds. Since panel holography typically takes six or more hours to complete, it is important that the antenna pointing be stabilized to better than ~ 10 arcseconds over this time period. Experience shows that VLA antenna pointing can ‘wander’ by values larger than this over such durations (especially if observations are taken through sunrise or sunset, or at high elevations), so it is critical that the pointing offsets be measured and corrected regularly via ‘referenced pointing’ which is normally accurate to considerably better than 10 arcseconds. The holography function in the OPT includes this capability. Pointing errors that are not due to differential temperature effects have a scale size on the sky of perhaps ~ 15 degrees, so in practice, referenced pointing is repeated approximately hourly.

2.2.6 Conversion to Panel Offsets

The phase image of the ERA, following correction of optical alignment errors, reflects the perturbations due to deviations of the reflecting surface(s). Ignoring for now the effects of errors in the subreflector surface, we can convert the phase to a physical length change in the main reflector. For a panel offset by ϵ millimeters in a direction normal to its surface, the phase change for normal incidence is

$$\phi = \frac{4\pi\epsilon}{\lambda} \quad (34)$$

radians. If the panel is tilted by an angle θ , the phase change is reduced by $\cos\theta$. Hence, the conversion to panel offset, normal to the antenna surface, is

$$\epsilon = \frac{\lambda\phi}{4\pi \cos\theta}. \quad (35)$$

The program HOLOG makes this correction when computing the panel displacement image.

3 Holography Measurement Methodology

The following setups for VLA antenna holography are now standard.

3.1 Observation Parameters

- **Observing Band** Ka-band is now the preferred band for dish holography. Although it is always best to utilize the highest frequency band available (since the effects of misshaped reflectors is greatest at that band), the vagaries of atmospheric phase stability and antenna pointing variations, combined with the poor sensitivity of Q-band, argue for Ka-band. The adjacent location of these feeds (separated by only 20 degrees around the secondary feed ring) minimizes the effects of subreflector shape errors.
- **Source Selection** Strong point sources are always preferred, especially at the highest frequency bands, where the antenna sensitivity S_a is poor. A minimum flux density of 5 Jy will ensure enough SNR for a good measurement. Extended (resolved) target sources can be used, provided their angular size is much less than the antenna beamsizes.
- **Elevation Range** It is preferred that the measurements be made near the median elevation of scientific observing – near $E = 50^\circ$, so the antenna efficiency will be maximized at this elevation. As there is evidence that the antenna surfaces change shape with elevation due to gravity, it is advisable to minimize the elevation range during the

observations. Unfortunately, astronomical sources generally change elevation significantly over the course of the ~ 6 hours needed for a full holography measurement. Of the strongest sources, 3C84 (J0319+4130) and 3C345 (J1642+3940) transit at too high an elevation, and change elevation by over 30 degrees during a six-hour duration, so are generally not employed. 3C273 (J1229+0203) is better – transiting at 60 degrees elevation, and with a maximum elevation range of 20 degrees if observed over six hours centered on meridian transit. There are a good number of 5+ Jy calibrators near zero declination which can be utilized, depending on the LST range available for the observations. Best are sources above a declination $\delta > 70^\circ$, but the strongest of these – J0217+7349, J1800+7828, and J1927+7348 – are all near 2 Jy at Ka-band. For these sources, use of multiple reference antennas and multiple spectral windows may be needed.

- **Preferred Configurations and Times** Since self-calibration is not an option in holography, very good phase stability is required. For the highest frequency bands, sufficiently good phase stability can only be assured in C or D-configurations, and on winter nights in calm, clear weather. Late night-time observations are always preferred, to minimize the effects of solar heating and radiational cooling of the antenna surfaces.
- **Reference Antennas** In general, use of multiple reference antennas is recommended. If all antennas are to be surveyed, then two separate runs will be required, with half the antennas designed ‘reference’ and half ‘target’. These designations are reversed for the second run. Alternating reference and target antennas on each arm minimizes phase perturbations. It can be useful to designate one antenna as a target on both days, in order to compare results.
- **Calibration Cadence** It is important that antenna pointing variations be minimized and that any atmospheric or instrumental phase variations be tracked. As argued above, variations in pointing must be much smaller than the grid spacing (typically 80 arcseconds) during the course of the observation, so we must utilize referenced pointing corrections at least hourly. Phase and amplitude calibration scans are needed much more frequently – the established procedure is once every two scans. With a 43 point raster length, on-axis calibration is done every 14.3 minutes.
- **Oversampling** Oversampling helps sensitivity, but increases the observation duration. Due to our use of a regular measurement grid, the derived images will suffer from aliasing. To minimize this, 20% oversampling is recommended.
- **Raster Movement** Although VLA antenna motion in azimuth is faster than in elevation, the potentially very large azimuth motions for low-frequency, high-resolution holography at high elevation encourage the major (initial) raster motion to be in the vertical. At the high frequencies used for dish holography, stepsizes are always small, so this argument is generally moot – nevertheless, we prefer to keep the primary motion in elevation.
- **Integration and Dwell Times** At the higher frequencies, where stepsizes are small, three seconds are needed for the antenna to move and reasonably settle. Dwell times per position of less than 10 seconds are thus not cost-effective, so ten seconds is the established standard. Integration (dump) times of 1 second minimize losses due to antenna motion, and enable finer data editing.
- **Number of Spectral Windows** The VLA’s correlator can span a tremendous bandwidth – up to 8 GHz. At lower frequencies, the SNR is sufficient even with ~ 2 Jy calibrators that only one or two spectral windows are needed. At Q-band, where SNR can be low if a northern source is taken as target, it would be prudent to retain at least eight spectral windows. Separate images for each spectral window are made, and averaged. At Ka-band, which is now the settled standard for VLA panel adjustments, a single spectral window is sufficient for a 5 Jy target source with two reference antennas (one on each side of the target antenna). Correlating two spectral windows, one from each of the two analog chains, would be prudent.
- **Polarization** Antenna panel holography requires only the Stokes ‘I’ data. Beam holography (where the goal is to accurately determine the angular structure of the primary beam and inner sidelobes for all correlation products), will generally utilize all four Stokes correlations, for which observations over a wide parallactic angle, and observation of a strongly linearly polarized calibration source with known position angle, will be required. The subject of full polarization beam holography is beyond the scope of this memo.
- **Raster Step Size** The raster step size is equal for both directions, and is set by

$$\Delta l = \frac{\lambda}{fD} = \frac{0.2997925}{fD\nu_G} \quad (36)$$

where f is the oversampling factor, D is the antenna diameter, λ the wavelength (in the same units as the diameter), and ν_G is the frequency in GHz. Assuming an oversampling of $f = 1.2$, (which is our standard for antenna surface holography), and an antenna diameter of $D = 25$ meters, the raster step increment in radians is

$$\Delta l = \frac{9.993 \times 10^{-3}}{\nu_G} \quad (37)$$

where ν_G is the frequency in GHz. In more familiar units, this becomes $34.1/\nu_G$ arcminutes. The frequency used by the on-line software to compute the offset stepsize is the center frequency of the higher-frequency baseband⁹, except at P-band, where the frequency is the lowest frequency in the baseband. This is an important consideration when designing a wideband holography experiment, since with our wide bandwidth systems, selection of an increment close to critical for the low frequency end of a band will result in significant undersampling of the beam pattern at the high frequency end. The current procedure is to select an oversampling factor such that the high frequency end of the band meets the desired oversampling factor of 1.2. The lower frequency end of the band could then be highly oversampled (by up to a factor of 2.4). The maximum angular offset needed to provide the desired resolution is then set by the lower frequency end – resulting in an image up to twice the desired physical resolution at the high frequency end.

For normal, high-frequency antenna holography where two, or a few, adjacent spectral windows are utilized, placing these around the high-frequency baseband frequency is best.

3.2 Software Programs Utilized

Here I describe the programs utilized in the antenna holography methodology.

3.2.1 Observing Script

Script generation is through the standard OPT, which understands the holography mode. Figure 4 shows typical inputs. We always utilize square grids, with an odd number of rows and columns. Panel holography is best done with at least a 43 x 43 raster, which gives better than 1 meter resolution. We have settled on using Ka-band (27 – 40 GHz) as the frequency of choice, with a center frequency near 33 GHz. Ten seconds per pointing is sufficient, providing the target source has at least 5 Jy flux density. For this band, it is advisable to use 3C273 (= J1229+0223) if possible, or another strong source near zero declination, as the range in elevation of the necessary six hours can be kept to 20 degrees by observing centered on meridian transit. If the source has at least 5 Jy in flux density, only two spectral windows are required. Oversampling of 1.2 is standard. If a larger holography grid is desired, It is advisable to schedule the observations over two days.

On the right side of the figure, under ‘Holography Grid’, are two qualifiers with the same name – ‘Initial Direction’. The first specifies the starting corner: ‘Left’ and ‘Down’ means the initial point will be the bottom left corner of the (l, m) grid. The second ‘Initial Direction’ indicates the primary (initial) basketweave scanning motion. In terms of the actual antenna motion in azimuth-elevation angle space, specifying ‘down left’ means the antenna will physically move to higher azimuth and higher elevation (providing the overall grid is centered on the source) – this is because the (l, m) coordinates are defined w.r.t. the antenna beam center. Sampling the lower left portion of the beam means moving the antenna to the right and up.

The raster pattern always starts at the specified corner and progresses in a basketweave pattern, ending at the diagonally opposite corner (if N is odd). Offsets of the raster pattern are possible – and necessary if a very large holography is to be kept within a small elevation range. For example, a 49 x 49 raster will take nearly 8 hours to execute, over which time the calibrator will change elevation by many tens of degrees. Since the antennas are believed to deform significantly with elevation, it is best to subdivide such a long raster over two or more days, each spanning a much narrower range in time/elevation. The two half-grids are then separated using the ‘offset’ command shown in the ‘Holography Grid’ panel.

Note that referenced pointing need not utilize the same frequency band as the holography observations. Most of the remaining inputs to the holography function in the OPT are self-explanatory, but the effect of one of these needs to be emphasized. In the left panel of the figure, under ‘Mode Dependent Settings’ is a box for ‘Max. Time (Hours)’. This is a ‘kill switch’ which will terminate the SB after the duration given. It is important that a duration significantly in excess of the expected maximum duration of the run be entered here.

⁹Note: This is not generally the center of any one of the spectral windows utilized in the observation. Commonly, it will be the frequency between the fourth and fifth spectral window.

The screenshot shows the 'Obs Prep Tool' interface. The 'SCAN DETAILS' section includes fields for NAME (J1229+0203), SCAN MODE (Holography), TARGET SOURCE (J1229+0203), HARDWARE SETUP (Holo-Q-Pair5), SCAN TIMING (Duration: 01:30:04), and INTENTS (MAP ANTENNA SURFACE). The 'ANTENNA WRAP' section is set to 'No Preference'. The 'MODE DEPENDENT SETTINGS' section shows 'MAX TIME (HOURS): 2.0' and a 'Reference Antennas' table with columns 0-9 and rows 00+, 10+, 20+. The 'Holography Grid' section has fields for Number of Points (21), Oversampling (1.2), Initial Direction (Left), Offset (0), Initial Direction (Elevation), and Dwell Time (10.0). The 'Intertwined Calibration & Pointing' section has sub-sections for Calibration (Holo-Q-Pair5) and Pointing (Flux2013-X1-RefPnt), both with 'Import' buttons, and fields for Duration (20.0) and Interval (4).

Figure 4: Inputs to the Holography Function in the Obs Prep Tool

3.2.2 Calibration

Calibration is by standard techniques. We normally assign a flux density of 1 Jy to the target source, as the absolute flux density is of no particular value. Partially resolved target sources can be used, but it is advisable to utilize a source model in the calibration step. Polarization calibration is not needed, unless the observation goal includes determination of the antenna beam polarization parameters.

3.2.3 Extraction to a Text File – UVHOL

The calibrated data are extracted for holographic processing by using the AIPS program UVHOL, which understands the special holography mode data formats. Shown below are the typical inputs to UVHOL needed for extraction of the data for processing by HOLOG.

```

UVHOL      Prints/writes holography data with calibration
Adverbs    Values      Comments
-----
INNAME     'AHOL-27MAY20'   Input UV file name (name)
INCLASS    '43TYAP'             Input UV file name (class)
INSEQ      1                   Input UV file name (seq. #)
INDISK     2                   Input UV file disk unit #
SOURCES    'HOLORASTER'        Sources to print, ' '=>all.
           *rest ' '
QUAL       -1                 Qualifier -1=>all
CALCODE    ' '                 Calibrator code ' '=>all
STOKES     'IV'               'FULL' in HOLG for 4 output
           files, 'IQUV', 'IV' also
SELBAND    -1                 Bandwidth to select (kHz)
SELFREQ    -1                 Frequency to select (MHz)
FREQID     -1                 Freq. ID to select.
TIMERANG   *all 0             Time range to select
ANTENNAS   9                 *rest 0             Reference antennas
BASELINE   2                 *rest 0             Moving antennas
SUBARRAY   0                 Subarray, 0 => 1
ICHANSEL   5                 60                 Spectral channels to average
           *rest 0
BIF        8                 IF number to print
DOCALIB    1                 > 0 calibrate data & weights
           > 99 do NOT calibrate weights
GAINUSE    0                 CAL (CL or SN) table to apply

```

DOPOL	1		If >0 correct polarization.
PDVER	0		PD table to apply (DOPOL>0)
BLVER	-1		BL table to apply.
FLAGVER	0		Flag table version
DOBAND	1		If >0 apply bandpass cal. Method used depends on value of DOBAND (see HELP file).
BPVER	0		Bandpass table version
SMOOTH	*all	0	Smoothing function. See HELP SMOOTH for details.
NCOUNT	0		# of sample. 0 => 1 page.
WTUV	0		Scale UV (actually LM) by WTUV, 0 => 1 in HOLG, else 0 => 1000
OPTYPE	'HOLG'		Choice of format type: 'HOLG' write holography file 'PLOT' plot holography data new else print holography data
NPOINTS	6		Number of samples to keep at the end of each pointing Used if APARM(1) = 0 0 => 100
APARM	0	0	(1) 0 => NPOINTS used
	0	0	1 => APARM(2,3) used
	1	1	(2) number of samples dropped at the beginning of each pointing
	*rest	0	(3) number of samples dropped at the end of each pointing
			(4) > 0 write elevation and azimuth at beg/end of scan
			(5) > 0 => average data over reference antennas
			(6) > 0 => average each pointing over time
			(7) > 0 => display real/imag in 'HOLG' and 'PLOT'
			(8) > 0 => average data over moving antennas
			(9) > 0 => scalar amplitudes in time & antenna average
			(10) > 0 -> apply parallactic angle correction on DOPOL
BDROP	0		Minimum number of samples to keep the pointing at all
DPARM	*all	0	1 : <0 => Range of (U,V,W), amplitude and weight is determined automatically; >= 0 => Ranges are fixed minimize the run time. 2 : Maximum weight; 0 => 99.0 3 : Minimum weight; 0 => 0.11 4 : Maximum amplitude; 0=>9.9 5 : Maximum of ABS(U),ABS(V), ABS(W) in klambda; 0 => 10000 6 : > 0 -> PLOT data as power in db (20*log10) > 1.5 if 2 moving ants in db (10*log10) 7 : > 0 plot phase or imag 8 : > 0 solve sidelobes

```

10 : > 0 scale by flux in SU
DOCRT      1      > 0 -> use the terminal,
             else use the line printer
             > 72 => terminal width

OUTPRINT   ' '

Printer disk file to save
HOLG: area to write outputs
PIXRANGE   0      0      (2) > (1) -> fix plot scale
FACTOR     0      Scale dots by FACTOR
             < 0 => connect dots too
SYMBOL     0      Plot symbol number: 1 - 24
DO3COLOR   0      > 0 use color to separate
             polarizations
LTYPE      3      Type of labeling: 1 border,
             2 no ticks, 3 - 6 standard,
             7 - 10 only tick labels
             <0 -> no date/time
DOTV       -1     > 0 Do plot on the TV, else
             make a plot file
GRCHAN     0      Graphics channel 0 => 1.
XYRATIO    0      X/Y ratio 0 -> fit TV or 1 PL
BADDISK    *all 0  Disk to avoid for scratch.

```

The reference antennas are selected under the ‘ANTENNAS’ adverb, the target antennas are selected by the ‘BASELINES’ adverb. Only one spectral window can be processed at a time, and is selected by BIF. Spectral averaging is standard over a single spectral window, and is specified by ICHANSEL. For high frequency holography, the full 128 MHz of any given spectral window can be averaged without significant image smearing. If more bandwidth is needed, multiple SPWs will need to be individually processed and the resulting files concatenated, or the transformed images averaged. Typically, NPOINTS=7 (7 seconds averaging with 1-second dumps) will prevent data taken while the antennas are moving from being included in the average.

The extracted data are written to an ascii file with name specified by OUTPRINT if OPTYPE = ‘HOLG’. (If OPTYPE = ‘ ’, it writes to the terminal screen). There are useful conventions for specifying the output file name – refer to the HELPFfile for explanation. APARM(7)=0 specifies the output to be amplitude and phase (=1 gives real and imaginary) which are needed for processing by HOLOG.

The calculations involved in the UVHOL step are very lengthy, so if repeated use of this program is envisaged (for example, if different target antennas utilize different reference antennas), then it is highly advisable to run SPLAT to generate a database in which the data are already calibrated, and the spectral averaging done. UVHOL would then run on this derived database, with the calibration and spectral selection turned off.

A snippet from a typical output file from UVHOL is shown in Figure 5 At the top of the file are written some useful ‘metadata’ describing the contents and origin of the data. In the following part, the first two columns give the l and m offset values, in radians (or, to be more precise, the inverse sine of the offset angle). In this example, all the l values are zero, so the data shown come from a vertical cut through the beam center. The next two columns give the moving antenna beam amplitude and phase. Note the beam values at ($l = 0, m = 0$) are near unit amplitude and zero phase, indicating the data have been calibrated. The final two columns give estimated errors in these quantities, driven from the scatter in the observed amplitudes and phases.

UVHOL has a useful plotting function, set by OPTYPE = ‘PLOT’ allowing display of the data on the terminal screen, or recording to a plot file. Although normally used for the beam cut data used for subreflector adjustment (see EVLA Memo 211 for examples), this may be useful for viewing wider angle data as well.

3.2.4 Image Formation – HOLOG

The data extracted by UVHOL are written to a text file. These data are then read in by HOLOG, which executes the Fourier transform, generating the images of the electric field amplitude over the antenna equivalent radiating aperture. HOLOG solves for and removes the phase errors caused by optical misalignments (antenna pointing and subreflector offsets). The program has numerous outputs, selected by the DPARMs, including the original gridded (‘beam’) data, the PSF, the Fourier inverted E-field weighting, and the oversampled power beam and its phase, with the effects of misalignments removed.

Typical inputs are shown below.

```

#! RefAnt = ** Antenna = 20 Stokes = 'I_' Freq = 31.807000000 DATE-OBS = '20170410'
#! MINSamp = 0 Npoint = 7
#! IFnumber = 3 Channel = 32.5
#! TimeRange = -99, 0, 0, 0, 999, 0, 0, 0
#! Averaged Ref-Ants = 19, 23,
#! DOCAL = T DOPOL = -1
#! BCHAN= 5 ECHAN= 60 CHINC= 1 averaged
#! LL MM AMPLITUDE PHASE SIGMA(AMP) SIGMA(PHASE)
0.0000000 -0.0072677 0.0369286 -174.4818878 0.0004316 0.6765018
0.0000000 -0.0069649 0.0445340 171.4394836 0.0004366 0.5891218
0.0000000 -0.0066621 0.0345682 153.9975739 0.0004322 0.7295464
0.0000000 -0.0063592 0.0180897 118.7108994 0.0004331 1.3939435
0.0000000 -0.0060564 0.0118955 -98.2106094 0.0004414 2.1252382
0.0000000 -0.0057536 0.0185267 -116.9897766 0.0004528 1.3329190
0.0000000 -0.0054508 0.0201834 173.9630280 0.0004205 1.1990825
0.0000000 -0.0051479 0.0286094 144.1610107 0.0004279 0.8507413
0.0000000 -0.0048451 0.0280940 96.3062744 0.0004350 0.8869567
0.0000000 -0.0045423 0.0178339 148.2498779 0.0004120 1.3996830
0.0000000 -0.0042395 0.0445103 179.0309448 0.0004425 0.5632897
0.0000000 -0.0039367 0.0514323 169.2209625 0.0004287 0.5127078
0.0000000 -0.0036338 0.0475517 179.9916382 0.0004590 0.5283867
0.0000000 -0.0033310 0.0554842 -178.9368896 0.0004511 0.4710984
0.0000000 -0.0030282 0.0623723 -174.9104919 0.0004601 0.3982278
0.0000000 -0.0027254 0.0419563 -165.5886536 0.0004175 0.6016617
0.0000000 -0.0024226 0.0487363 -153.0545197 0.0004490 0.5361019
0.0000000 -0.0021197 0.0542334 -154.2506409 0.0004491 0.5017058
0.0000000 -0.0018169 0.0174415 -112.7214050 0.0004499 1.4626453
0.0000000 -0.0015141 0.0712320 -163.9234161 0.0004438 0.3868665
0.0000000 -0.0012113 0.1461334 -170.2458954 0.0004269 0.1735736
0.0000000 -0.0009085 0.1800243 -171.6838989 0.0004592 0.1974622
0.0000000 -0.0006056 0.0878549 -145.6300964 0.0005671 0.3676832
0.0000000 -0.0003028 0.6225165 -4.3898258 0.0004646 0.0888120
0.0000000 0.0000000 1.0001020 -1.0394337 0.0005244 0.0878493
0.0000000 0.0003028 0.2785297 -20.8832779 0.0006836 0.2248604
[rperley@LOCALHOST ~]$

```

Figure 5: Typical output from UVHOL, showing the initial ‘metadata’, and a few lines of the first vertical raster scan.

```

HOLOG: Task to read and process holography visibility data
Adverbs Values Comments
-----
INFILE 'EA28-MAY20-I_04'
Input data file name.
OUTNAME '28-2020-PNT'
Output image name.
OUTDISK 2
Output disk number.
UVTAPER 0 0
Data tapering: (1) type,
(2) width in cells to 0.5
OPTYPE 'SURP'
Telescope type: 'PFOC' prime
focus, 'SUBR' subreflector
'SURP' subreflector with
reference pointing
FACTOR 13
Magnification: 0 -> 13
REFREQ 0
Reference frequency in GHz
APARM 0 0
Operating parameters.
25 4
1: Frequency (GHz).
8.8 0.7
2: Satellite elevation, deg.
*rest 0
Use 0 for sidereal obj.
3: Antenna diameter, m.
4: Unpaneled diameter, m.
(3,4) used to blank ant.
aperture phase data.
5: Focal length, m.
6: Slope in SURP 0 -> 0.65
7: Disabled
8: Disabled

```

```

9: 10000 * Ref ant. +
   100 * target ant. + IF#.
10: Stokes (RR=1, LL=2)
    (9) and (10) used only
    if INFILE is not of form
    'AREA:FILE'

BPARM      30      256      Data reduction parameters.
           0        0      1: Required map size, meters
           0       -2      2: No. of pixels on a side
          -2     -12      of the output map (power
           0        0      of 2, min=32, max=512).
                                0 => 128
           0        0      3: Min. antenna scan angle
                                Units: inverse sine(ang)
                                0 => all data used.
           0        0      4: Max. antenna scan angle
                                Units: inverse sine(ang)
                                0 => all data used.
                                <0 => radial (min, max).
           0        0      5: Amplitude scaling factor
                                0 => 1
           0        0      6: Fourier transform sign
                                0 => -1 (VLA convention)
           0        0      7: Minimum antenna aperture
                                used for fit, in meters
                                < 0 => circular min.
                                0 => set by APARAM(4)
           0        0      8: Maximum antenna aperture
                                used for fit, in meters
                                < 0 => Circular max.
                                0 => set by APARAM(3)
                                (7,8) used for focus and
                                pointing calculations.
           0        0      9: Correction control flags:
                                read the HELP!
           0        0      10: >0 => logarithmic ampl.
                                .LE. 0 => linear ampl.
                                default = linear

CPARM      1        0      Parameters for the gridding
           0        0      operation (see HELP).
           0        1      *rest 0
NORMALIZ   0        0      > 0 => normalize outputs 1
                                and 2 below
DOVECT    -1        0      > 0 write real/imaginary not
                                amplitude/phase images
DPARAM    0        0      Output maps, >0 => Save this.
           0        1      1,2: Regridded amplitude and
           0        0      phase of the observed
           0        0      antenna beam pattern.
           1        0      3: Weights used in the
                                regridding procedure.
           0        0      4,5: Derived amplitude and
                                phase of the antenna
                                illumination
           0        0      6,7: Amplitude and phase of
                                the point-spread func.
           0        0      8: Focus model corrections
           0        0      9: Surface deviation map.
           0        0      10: Antenna power pattern
                                (See HELP!)

VPARAM    *all 0      Use this model don't fit
           0        0      1. Constant offset degrees

```

2. Phase ramp in X deg/cell
3. Phase ramp in Y deg/cell
4. Feed offset X in mm
5. Feed offset Y in mm
6. Feed offset Z in mm
7. Subreflector X tilt mm
8. Subreflector Y tilt mm
9. > 0 replace phase w model
10. > 0 Replace amp with average, value is clip level (all below set 0)

Use of the adverb values shown above will result in optimum results. Some require extra explanation, given below.

BPARAM(6) is an important parameter – if set to -1, it will do an FFT of the observed data, thus requiring gridding of the data. If set to -2, the inversion is via a direct (or discrete) transform. (The sign refers to the phase convention – negative is correct for the VLA data). Use of a direct transform is strongly recommended as gridding the near critically-sampled data will generally result in blank rows and columns in the gridded plane, leading to uncertain results. There is little difference in execution speed (as the transforms are very modest, with typically 2500 points), and a large advantage in avoiding issues with the regularly sampled observation grid in (l, m) not aligning with the grid required for the FFT.

BPARAM(7) and BPARAM(8) set the minimum and maximum radii within which the derived aperture phase and amplitude images will be used in solving for the antenna optics corrections. The values shown ensure that edge effects will minimally affect the phase corrections.

OPTYPE specifies the optics model to be employed for removal of pointing and subreflector offsets. Setting this to ‘SURP’ is appropriate for observations which utilize referenced pointing to center the primary beam. In practical terms, it fits the model given in equation 16, as shown in the right-hand panel of Figure 2, rather than equation 15, and shown in the center panel.

Using a DFT (BPARAM(6) = -2) allows generation of the output images of the illumination amplitude and phase, and antenna surface deviations (DPARMs 4, 5, and 9) independent of the (l, m) grid sampling. However, if images of the observed raster beam data are desired (DPARMs 1, 2, and 3), care must be taken to set the aperture image size (BPARAM(1)) to the value which ensures that the grid spacing in the images matches the stepsize used in the observations. The value to be used is given by: $BPARAM(1) = 25f\nu_G/\nu_{SPW}$, where ν_G is the frequency used to set the observation grid spacing, (see the text following equation 37 for details), f is the oversampling factor, and ν_{SPW} is the center frequency of the spectral window whose data are to be displayed. For these displays, it is also important to set the CPARMs as shown to prevent smoothing the sampled data on the grid.

If the panel offset is larger than a half-wavelength, the derived value may suffer from an ambiguity where the true value is a wavelength greater, or less, than the correct value. The presence of this ambiguity can only be found through examination of the panel phase or displacement image. The characteristic is a step of one wavelength (or more – due to the curvature of the antenna surface) in the output panel displacement image. If the sign of the ambiguity can be determined by examination of the phase image, the data can be corrected by using the AIPS functions PRTIM (to print out the panel values) and PUTVAL to add, or subtract one wavelength (divided by cos angle). This problem is much less severe now, as all major panel adjustments were completed before 2000.

3.3 HOLOG Example Outputs

The operations described above should be clearer by examining example images from HOLOG. For these, we use the 43 x 43 raster data taken at X-band on 31 Dec 2014, with 1.2 oversampling.

The sampled angle coverage (provided with DPARM(3)=1, point-spread function amplitude (DPARM(6)=1) and two cuts through this image, are shown in Fig. 6. Note that the high sidelobes in the PSF are due to the use of an unweighted transform. These sidelobes can be considerably reduced, at the cost of spatial resolution, by using the tapering function ‘UVTAPER’ in HOLOG. Experience has indicated that the unweighted transform, combined with the oversampling factor of 1.2 result in minimal perturbations in the panel images, despite the high PSF sidelobes.

A direct transform of the 1849 measured beam amplitudes provided images of the ERA. The amplitude and phase of this transform are shown in Figure 7.

After generating the transforms, the HOLOG program then solves for the optical alignment errors, using the expressions derived by Ruze. (For a full description see the appendix of EVLA Memo #121). The antenna phase surface is then corrected for the offsets, and the resultant converted to panel offsets, utilizing the expression in eqn 35. The model, and the final panel image are shown in Figure 8. An example output from the solution is shown in the left side of Fig 9.

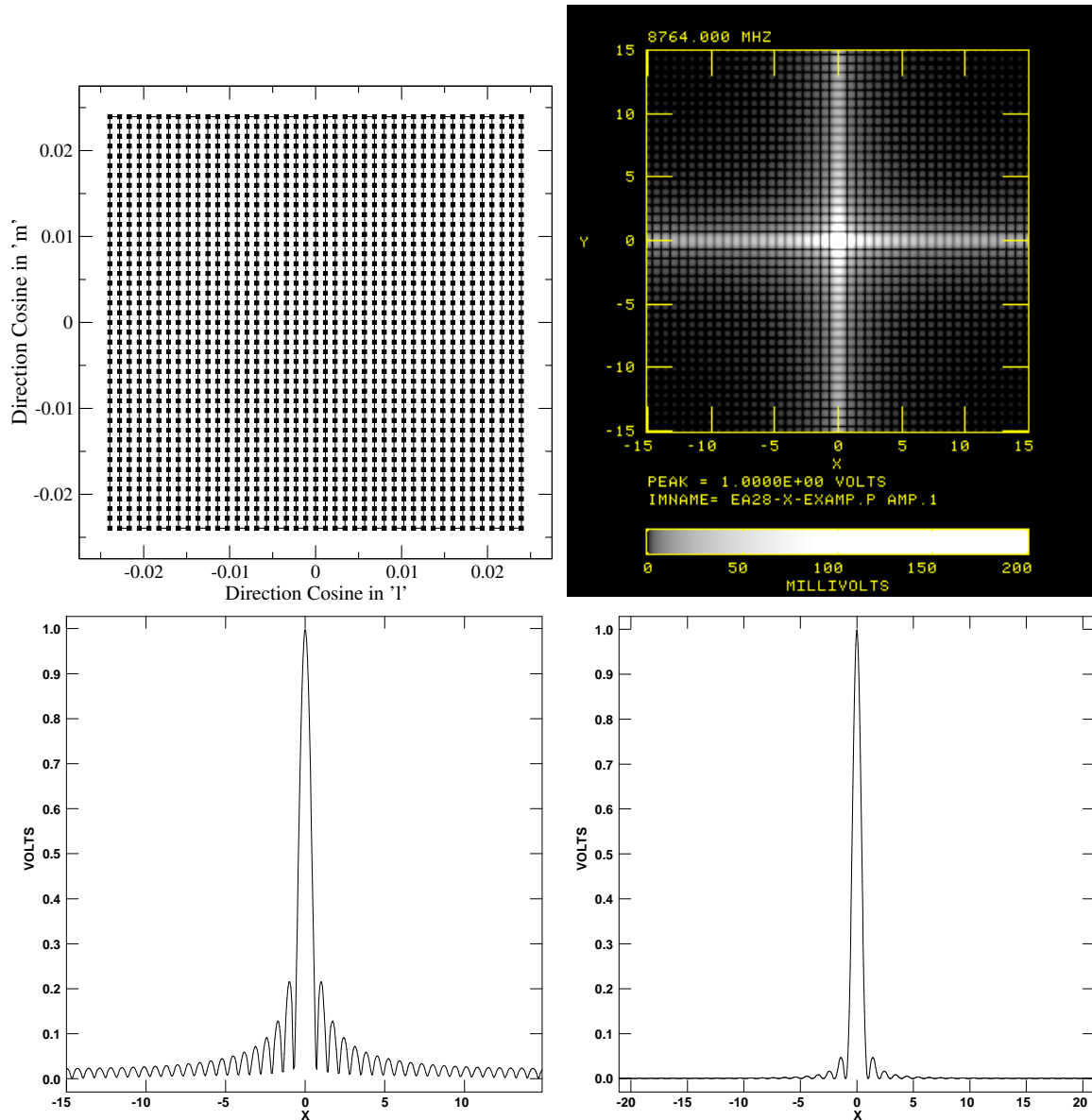


Figure 6: Results from a 43 x 43 holography run taken at X-band with 1.2 oversampling. Shown are results from 8.764 GHz. Upper Left: The offset angle coverage. Observations started in the lower left, and terminated at upper right, following the line connecting the points. Upper Right: The resolution beam (PSF) from the sample grid. Lower Left: A horizontal cut through the PSF. Lower Right: A diagonal cut through the PSF. Scales are in meters. The resolution is 0.85 meters.

3.4 Conversion to Panel Setting Changes: PANEL

The outputs from HOLOG are in the form of AIPS image files. The panel offsets (produced by $\text{DPARM}(9) = 1$ in HOLOG) must be converted to vertical displacements for each of the four threaded screws which adjust the corners of each panel. The calculations for this are done by the AIPS program PANEL.

PANEL reads both the panel offset image, and the illumination amplitude image provided by $\text{DPARM}(4) = 1$ in HOLOG. This latter image is used in weighting the solutions. PANEL knows the VLA's panel layout, and offers three models for determining the offsets of the nuts on the threaded rods which adjust the panel corner positions. The models are: (1) Rigid panel – all values over the panel area are averaged, and a single displacement for all corners is produced; (2) Rigid/tilt – a slope and offset is determined for each panel, and the resulting vertical offsets for the four corners derived; (3) Flexible – four independent values are produced, one for each corner, without constraints. We normally choose the 'flexible' option – $\text{APARM}(1)=3$, but have not compared the results to the other two. The file named in 'OUTFILE' generates the file used by the antenna mechanics for adjusting the panels.

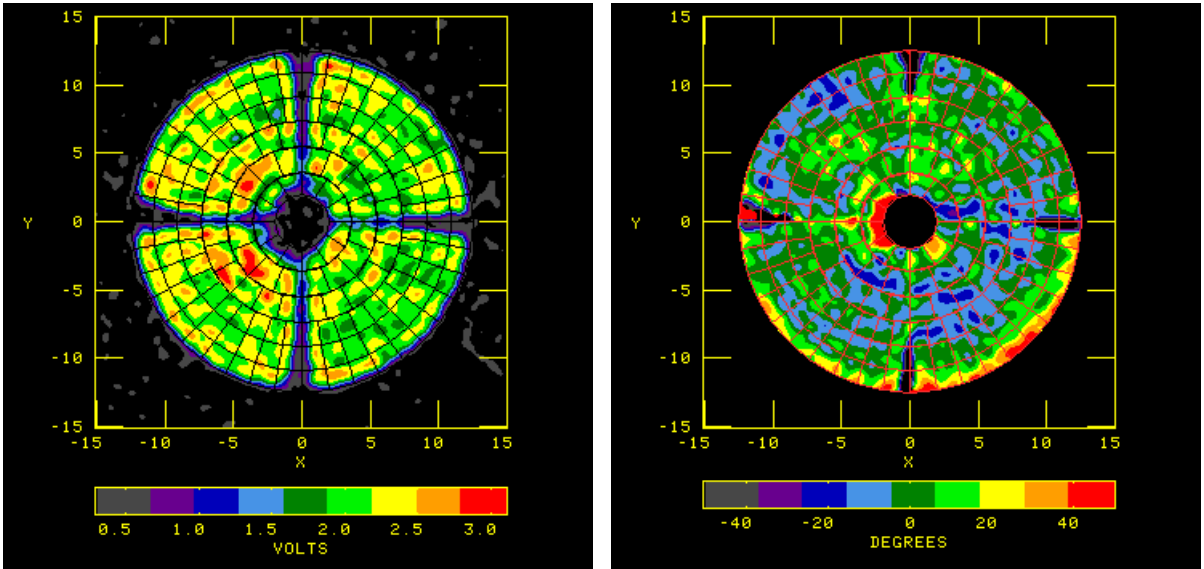


Figure 7: The raw amplitude and phase outputs from the HOLOG program. **Left Panel:** Amplitude – proportional to the aperture voltage illumination. The horizontal and vertical dark regions are due to shadowing from the quadrupod legs. **Right Panel:** Phase – including the effects of panel irregularities and large-scale errors from optics misalignments.

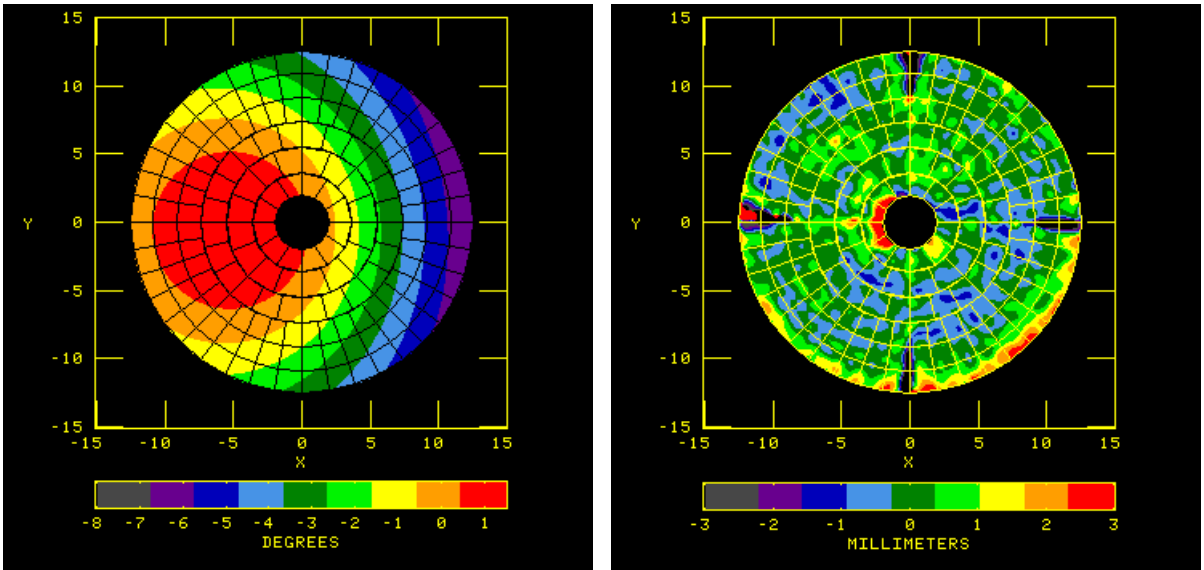


Figure 8: **Left Panel:** The model fit for subreflector position errors. For this antenna, the offsets are very small – 0.4 mm horizontal offset, and 0.6 mm focus error, so the corrections in terms of phase are less than 7 degrees. **Right Panel:** The panel offsets, following correction for the optical misalignment, and conversion to physical units, including accounting for the tilt of the panel.

Shown below is an example input to PANEL:

```
PANEL: Task to convert a HOLOG image to panel adjustments
Adverbs      Values      Comments
-----
INNAME       '28-2020-PNT'  First image name
INCLASS      'V_DEV'        First image class
INSEQ        1             First image seq. #
INDISK       2             First image disk drive #
IN2NAME      '28-2020-PNT'  Mask image name
IN2CLASS     'V_AMP'        Mask image class
```

```

1 HOLOG OUTNAME='EA02-64MHZ ' OUTCLASS='_V_DEV '
2 HOLOG OUTSEQ= 3 OUTDISK= 1
3 HOLOG Visibility file: HOME:EA02-2REF-64MHZI 03
4 HOLOG Visibilities used: 1849 of 1849
5 HOLOG Observing frequency: 33.319000 GHz, Wavelength: 0.008998 m
6 HOLOG Satellite elevation: 0.000 deg
7 HOLOG Antenna diameter: 25.000 m
8 HOLOG Subreflector diameter: 4.000 m
9 HOLOG Focal length: 8.800 m
10 HOLOG Map size: 35.000 m, 256 pixels
11 HOLOG Antenna scan angle range: 0.00000 0.00000 radians
12 HOLOG Amplitude scaled by: 1.000
13 HOLOG Fourier transform: DFT with phase negation
14 HOLOG Antenna surface range: -2.00000 -12.00000 m
15 HOLOG Interpolation type in l: 1.000 0.500 0.000 0.000 0.000
16 HOLOG Interpolation type in m: 1.000 0.500 0.000 0.000 0.000
17 HOLOG Output option flags: FFFFFFFF
18 HOLOG Subreflector with reference pointing Magnification: 13.00
19 HOLOG OFFSET = 0.5220 prime focus-bottom subreflector in m
20 HOLOG Slope for Q in SURP 0.700
21 HOLOG Amplitude Peak: 3.94866E+00
22 HOLOG Phase offset: -38.37 1.21 deg
23 HOLOG Equiv. Pointing Error in X: -0.05 0.00 arcmin
24 HOLOG Equiv. Pointing Error in Y: 0.09 0.00 arcmin
25 HOLOG Subreflector offset in X: 3.62 0.07 mm
26 HOLOG Subreflector offset in Y: -0.56 0.07 mm
27 HOLOG Subreflector focus error: 0.59 0.02 mm
28 HOLOG Subreflector tilt in X: 0.00 0.08 degrees
29 HOLOG Subreflector tilt in Y: 0.00 0.08 degrees
30 HOLOG Cassegrain offset in X: 0.00 0.74 mm
31 HOLOG Cassegrain offset in Y: 0.00 0.74 mm
32 HOLOG Weighted Half-path error: 0.369 mm.
33 HOLOG Measured gain: 78.13 dB
34 HOLOG Theoretical gain: 78.75 dB

```

```

Antenna = EA17 Date-obs = 20200527
Processed : 19-MAY-2021 10:24:50
Panel fitting option : Flexible panel
rms before adjustment : 0.25 mm
rms after adjustment : 0.18 mm
Estimated Gain Performance -- Uniform Illumination
-----
3.5cm 2.0cm 1.3cm 0.7cm 0.34cm
Uncorrected | 36.97 41.80 45.48 50.61 55.87
Corrected | 36.98 41.82 45.53 50.78 56.49
Theoretical | 82.13 86.99 90.73 96.11 102.38

```

Conventions in the following are
Units are (INCH/1000).
Rings are numbered from inner to outer
thus center to rim of dish
Panels are numbered clockwise, starting from
the highest point as seen from the front
looking into the dish
Lower means away from subreflector
Raise means toward the subreflector
LOWER the panel if the number is POSITIVE
RAISE the panel if the number is NEGATIVE

ring	panel	Inner edge		Outer edge	
		left	right	left	right
1	1	22.	-7.	13.	-9.
1	2	4.	-1.	5.	22.
1	3	-2.	-53.	0.	9.
1	4	-1.	3.	29.	-15.
1	5	-5.	-17.	-5.	-10.
1	6	17.	-40.	-17.	-10.
1	7	-17.	-5.	1.	-7.
1	8	1.	-25.	8.	2.
1	9	-43.	34.	9.	-23.
1	10	3.	-37.	19.	3.
1	11	-3.	-31.	13.	17.
1	12	-3.	10.	4.	23.
2	1	-1.	-15.	3.	-3.
2	2	6.	-1.	-6.	20.
2	3	-0.	12.	19.	-0.
2	4	-9.	11.	16.	-2.
2	5	0.	28.	2.	2.
2	6	24.	-12.	4.	5.
2	7	3.	1.	2.	-12.
2	8	-1.	2.	-18.	25.
2	9	-2.	7.	5.	-4.
2	10	14.	-14.	-12.	-4.
2	11	1.	15.	1.	-5.
2	12	21.	69.	-3.	10.

[rperley@LOCALHOST FITS]\$

Figure 9: (Left) Output from HOLOG, containing the parameter estimations from the model. (Right) Partial output from PANEL, showing the detailed offsets for each corner of each panel.

```

IN2SEQ      1      Mask image seq. #
IN2DISK     2      Mask image disk drive #
BLC         *all 0  Bottom left corner
TRC         *all 0  Top left corner
XINC        1      X pixel increment
YINC        1      Y pixel increment
OUTFILE     'EA28-2020-TLT' Panel adjustment file
DOPLOT      0      Bit map of desired plots
APARM       3      0.8 (1) panel model
              *rest 0 (2) clip level in Mask image
              (3) map size in meters
              (4) Frequency in GHz
              (5) number pointings (1 dim)
              (8) > 0 Suppress grey-scale
              (9) > 0 Suppress countour
              (10) > 0 Suppress layout

INLIST      ' , '   Text file with focus, layout
              ' , ' -> VLA, 'VLBA' known
DOTV        -1     > 0 -> AIPS plots to TV

```

```

TVCHAN      0          TV channel to use 0 -> 1
GRCHAN      0          Graphics channel to use

```

The first input image is the surface displacement image generated by HOLOG (DPARM(9) = 1), and the second input image is the illumination amplitude, generated with DPARM(4) = 1. APARM(2) is a blanking level – cells with an illumination amplitude less than this value will be ignored in the panel setting solutions. The OUTFILE contains the detailed adjustment values used by the antenna crew in making the adjustments. APARMs(3) to (5), if left at zero, are provided by the metadata in the input file given by ‘INNAME’, which is generated by HOLOG.

An example of the output from PANEL is shown in the right side of Fig 9: In this output is an estimate of the corrected and uncorrected gain, and a comparison to ‘theoretical’. There is clearly an error in these values (the gains at 3.5cm should be very close to ‘theoretical’). This has been remedied, so subsequent calculations will show reasonable values.

The PANEL program generates three plots which are useful in judging the fit quality. Examples from ea02 from the 2017 observations are shown in Fig 10. These figures (which are best viewed on the TV monitor) show the surface

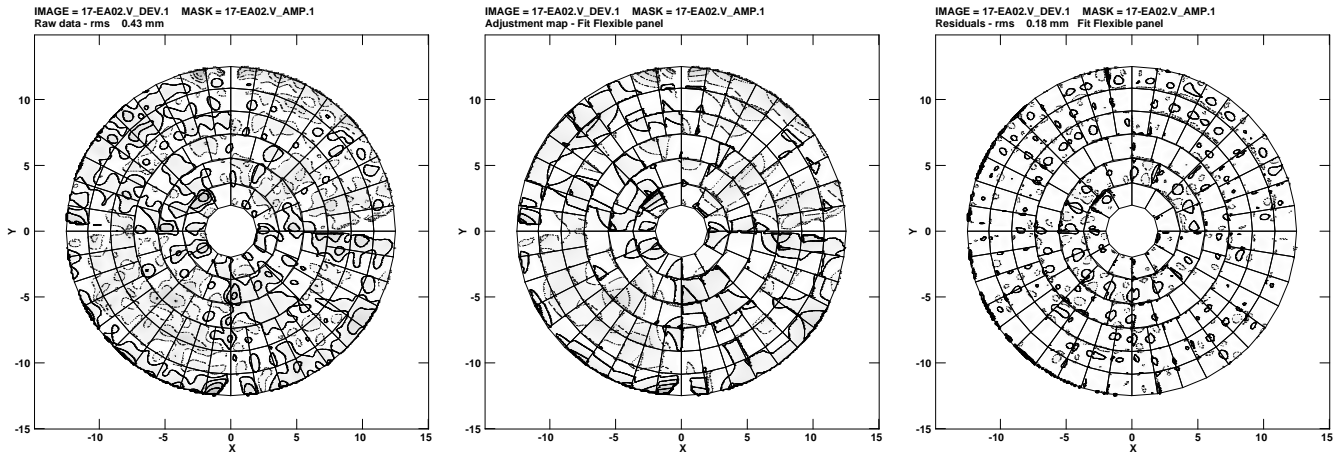


Figure 10: Showing the graphic output from PANEL. The left panel shows the surface deviations before fitting. The middle panel shows the model to be applied to the antenna panels. The right panel shows the result after the model is removed. The contour interval is 0.25 mm. The tendency for the largest deviations to lie towards the panel enters indicates panel curvature, which cannot be corrected by corner adjustments.

before and after fitting, with the model to be applied in the middle. The contour interval is hard-wired to 0.25 mm. An important observation is that the majority of the residual errors in the corrected image are in the central areas of the panels, indicating curvature (possibly temperature-sensitive) in the panels themselves. These cannot be corrected by adjusting the panel corners, and represent a fundamental limit to the accuracy of panel settings.

4 Panel Displacement Test

The first post-EVLA holography panel adjustment was attempted in 2016, on ea20, using data taken in February of that year. To our considerable chagrin, the post-adjustment figure was worse than before. After some review, it was clear that in the time since the last adjustments were made (16 years earlier), the signs in one or more programs, or in our understanding of the results, had been reversed, so that adjustments made on the ‘right’ side of the antenna were made using values for the ‘left’ side.

There are ample places in all of this for signs to get confused. With the uncertainties in sign conventions – both for the antenna raster motion, and in the Fourier transforms – we should be concerned that the surface image may be rotated about one of the principle axes, or that the sign of the displacement may be negated. The best way to check our conventions is to raise a panel by a known amount, then make a holographic measurement.

This test was done on 29 March 2017. Three panels on antenna ea18, located on pad W09, were displaced by known amounts, two upwards, (i.e., towards the subreflector), one downwards. To prevent sign ambiguities, the displacements must be less than $\sim 1/4\lambda$ – the values chosen were -3 mm for panel #9 on ring #4 and, +5mm for panel #8 on ring #3, and +4mm for panel #22 on ring #4. These panels were selected so none were under a quadrupod leg. A 31 x 31 holographic raster was taken at Ku-band (15 GHz), using the strong source J0854+2006, with the array in the ‘D’-configuration. The elevation ranged from 50 to 76 degrees during the observations.

The results are shown in Figure 11. The left panel shows the deduced displacements – the three modified panels are easily visible. The panel layout grid is superposed in yellow. The values determined for the offsets, relative to the adjacent panels, are within 0.5 mm of the known offsets. The right panel shows the engineering diagram, provided by Mike Romero, showing the location of the displaced panels.

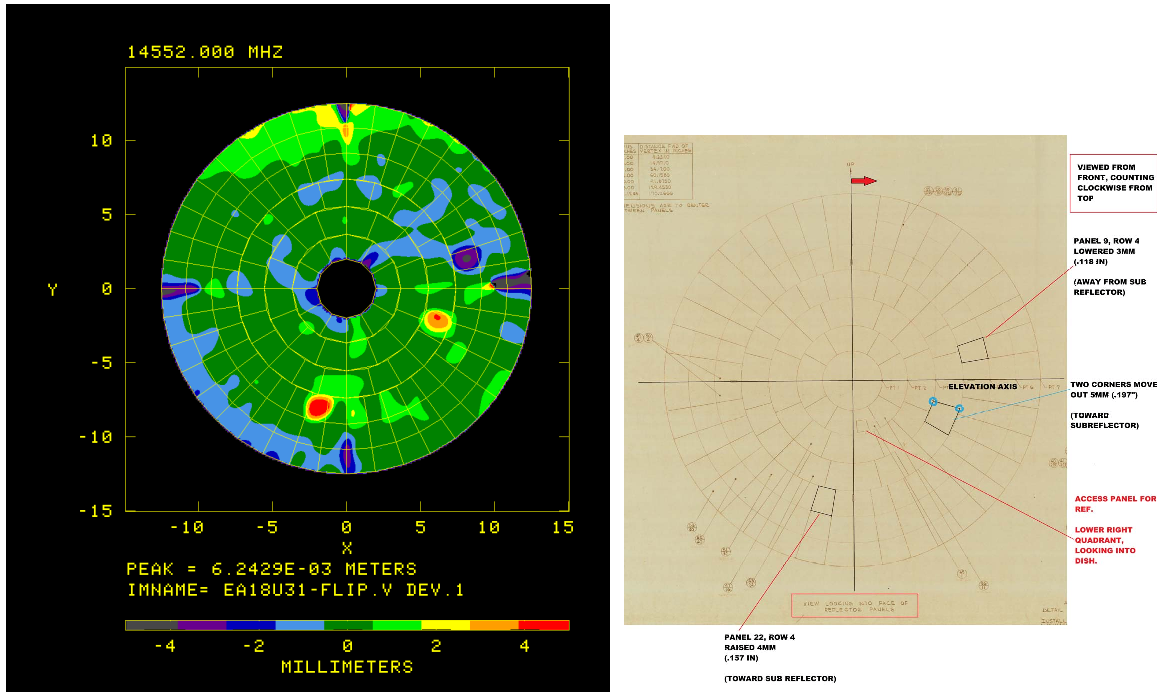


Figure 11: Showing the results from the test on ea18 from 29 March 2017. The left panel shows the measured displacements, in millimeters. Panel 9 on ring 4 was lowered by 4 mm. The upper two corners of panel 22 on ring 4 were raised 4 mm. Panel 8 on ring 3 was raised by 5mm. The observed offsets, relative to the surrounding panels, are in excellent agreement. The right figure shows the engineering plan, provided by Mike Romero.

We conclude that the panels are correctly identified, with the correct signs (positive offset means the panel is high (displacement is towards the subreflector), negative means it is low) and amplitudes, and that the images we produce correspond to viewing the antenna from the front, looking into the dish.

5 Holography Adjustment History

Original adjustment of the panels began in late 1994 and were completed in 2000. All antennas, except ea20, were adjusted using either Q-band or K-band observations. An early comparison of before and after gains by Mike Kesteven on the original adjusted antenna (ea04) indicated a gain improvement of 2 – 3 dB at K-band (and hence much more at Q-band). After a long hiatus, panel adjustments resumed in 2017, and are ongoing.

Table 1 gives the antenna panel adjustment history.

The first nine antennas to be adjusted, from 1992 to late 1995, were done based on measurements made at X-band – this band was chosen as the SNR is very much higher than at Q-band, while atmospheric phase errors and the effects of pointing errors, are much less. However, the improvements in Q-band sensitivity resulting from these early panel adjustments were not as good as expected, so that in early 1996, (following the suggestion from Durga Bagri), adjustments based on Q-band observations began, despite qualms about the stability of the pointing and atmospheric phase. The results from this were considerably better, so this band was used for all thirteen antennas then equipped with Q-band receivers. This was completed in early 1997. As the remaining 15 antennas were not equipped with Q-band receivers until 2000, the initial round of holography adjustments were completed using K-band observations. For reasons now lost, antenna ea20 was not adjusted using either Q or K band observations. The initial round of holography adjustments was completed by late 2000.

Table 1: Log of Surface Holography Adjustments

Antenna	X-Band	Q-Band	K-Band	Ka-Band
1			08 May 1998	06 Apr 2020
2			30 Nov 2000	
3		20 Mar 1996		
4	05 Jul 1993	10 Apr 1996		23 May 2018
5			28 Jan 1998	
6	17 Nov 1995	01 Apr 1996		
7			09 Mar 1998	
8		29 Mar 1996		
9			19 Dec 1997	
10			23 May 2000	
11	16 Nov 1995	08 Feb 1996		
12		03 Jan 1997		
13	21 Dec 1994	02 Feb 1997		
14	01 Dec 1994	06 Mar 1997		
15		14 Apr 1997		22 Aug 2017
16		29 Jan 1997		
17			11 Jul 2000	22 Aug 2018
18			15 Oct 1999	
19			03 Nov 1999	
20	15 Nov 1995			05 May 2017
21			23 Jul 1998	
22	14 Feb 1992	03 Apr 1996		
23			26 Jul 2000	
24			08 Jun 2000	
25	13 Feb 1995	27 Jun 1996		
26			25 Aug 1998	17 Jan 2019
27	15 Dec 1994	24 Apr 1996		
28			15 Jun 2000	

6 Post-EVLA Panel Adjustments

The EVLA Project introduced many changes to the antennas – including wholly new receiver bands, a new feed layout, and a new mounting system. Following completion of the implementation of the new receiver systems, and the availability of the new wideband ‘WIDAR’ correlator, it appeared prudent to re-survey the antenna surfaces, both to check on whether these changes had made significant changes to the reflector figure, and to repair any outstanding issues. Thus, the holography program was restarted in mid 2011.

There was some evidence from early photogrammetry work that the subreflectors impose a significant phase pattern on the main reflector. Since the subreflector rotates to a different position for each band, there is the possibility that doing holography at multiple bands would enable separation of the main reflector errors from the subreflector. Hence, we elected to do the new holography surveys at multiple bands – X, Ku, K, Ka, and Q. However, these multi-band data have not yet been analyzed for this purpose.

Significant software changes were also made to support the new holography imaging and to simplify the analysis. Michiel Brentjens (from ASTRON) spent five months here in 2011 implementing the Executor code which permits square (l, m) surveying at all elevations and offsets, and also rewrote the analysis code in Python. The intention was to have a standalone package to simplify the post-processing. However, this latter effort was not quite completed upon his return to the Netherlands, so we then elected to bring the standalone analysis programs written by Mike Kesteven under AIPS. The major advantage of this is retention of the full flexibility provided by AIPS in calibration and data review and presentation.

In 2016, it was decided to make the primary panel adjustments based on Ka-band observations. The main justification is its considerably greater sensitivity than Q-band, and its reduced sensitivity to antenna pointing problems and atmospheric phase instability. The Ka and Q band feeds are separated by only 23 degrees, which should minimize any differential effects due to the subreflector shape errors – changes made to the primary surface from Ka-band measurements should be largely similar to those required at Q-band.

Data for this program have been taken at X, Ku, K, Ka, and Q bands, as described in the log below. The four

Table 2: Chronological Log of Antenna Holography Observations

Date	Cnfg	Band	SPW	Source	N	ElRng	MST Time	Comments	
14 Oct 11	D	K	1	J0319+4130	41	46 – 82	22:20 – 03:15		
21 Oct 11	D	Q	16	J0217+7349	41	47 – 50	22:15 – 03:40		
22 Oct 11	D	Q	16	J0217+7349	41	40 – 49	23:20 – 04:40		
29 Oct 11	D	Q	16	J1229+0203	41	37 – 58	07:05 – 12:25		
30 Oct 11	D	Q	16	J2253+1608	41	38 – 72	18:35 – 00:20		
07 Nov 11	D	X	2	J2253+1608	41	48 – 72	17:15 – 22:50		
28 Apr 12	C	Ku	2	J0217+7349	41	43 – 50	09:50 – 15:20		
29 Apr 12	C	Ku	2	J0217+7349	41	40 – 50	07:50 – 13:20		
21 Dec 14	C	Ku	2	J0217+7349	43	43 – 50	18:30 – 00:10	Last 11 scans missing	
24 Dec 14	C	Ka	8	J0217+7349	43	41 – 50	18:15 – 00:05		
28 Dec 14	C	Ka	8	J0217+7349	43	39 – 50	18:35 – 00:25		
29 Dec 14	C	Ku	4	J0217+7349	43	40 – 50	18:15 – 00:05		
31 Dec 14	C	X	4	J0217+7349	43	39 – 50	18:13 – 00:07		
01 Jan 15	C	X	4	J0217+7349	43	37 – 50	18:40 – 00:33		
02 Jan 15	C	Ku	4	J0217+7349	43	43 – 50	17:26 – 23:07		
03 Jan 15	C	Ka	8	J0217+7349	43	43 – 50	16:58 – 22:50		snow
07 Jan 15	C	Q	16	J0217+7349	43	41 – 50	17:25 – 23:16		
17 Jan 15	CnB	Q	16	J0217+7349	43	44 – 50	15:57 – 22:48		
20 Feb 15	B	X	4	J0217+7349	35	42 – 50	12:50 – 16:48		Panel Test
27 Mar 16	C	Ka	8	J1256-0547	43	31 – 50	21:55 – 03:55		
16 Mar 17	D	Ku	16	J1459+7140	30	42 – 52	23:46 – 02:35	Panel Test	
22 Mar 17	D	Ku	16	J0854+2006	33	62 – 76	17:20 – 20:45	Panel Test	
29 Mar 17	D	Ku	16	J0854+2006	31	50 – 76	17:53 – 20:43	Panel Test	
10 Apr 17	D	Ka	16	J1256-0547	49	38 – 50	22:30 – 02:17	First Half	
16 Apr 17	D	Ka	16	J1256-0547	49	40 – 50	21:12 – 01:00	Second Half	
11 May 17	D	Ka	16	J1743-0350	49	41 – 50	01:00 – 04:50	First Half	
12 May 17	D	Ka	16	J1743-0350	49	38 – 50	01:20 – 05:10	Second Half	
20 Jan 19	C	Ka	8	J1058+0133	43	28 – 58	23:26 – 05:25		
21 Jan 19	C	Ka	8	J1058+0133	43	28 – 58	23:20 – 05:20		
18 May 20	C	Ka	8	J1743-0350	43	33 – 52	23:11 – 05:10		
27 May 20	C	Ka	8	J1743-0350	43	32 – 52	22:43 – 04:42		

observations at the top of the table include a 15x15 raster with $f = 4$ oversampling of the central beam, to the 2nd null. Time has dulled the memory of why so many ‘Panel Test’ observations were taken. Only the last, taken on 29 March 2017, was actually utilized. The 2017 observations are of higher resolution – 49 x 49 – and were split over two separate days to minimize low elevation observations. For each pair, the UVHOL outputs must be concatenated before executing HOLOG.

One of the observations made in the winter of 2014/2015 is not useable due to snow in the dishes. Snow and ice have a remarkable effect on the holographic images – large ‘holes’ in the E-field amplitude images due to absorption. In Fig 12 are shown the amplitude and panel displacement images for ea13 from data taken on 03 January, 2015. The effect of the snow is to absorb the astronomical signal, causing the surface to effectively ‘disappear’. All of the target antennas that day are affected – some much more than others. The snow tends to collect in the bottom half of the dish. Note that the effect of the absorption is to significantly modify the shape of the primary beam, as well as to reduce the forward gain and increase the system temperature due to thermal emission from the snow itself. A clear lesson for all observing is that high frequency observations should not be attempted if there is **any** snow or ice on the reflector.

7 Holography Results from the Second Round

In this section, I present some of the results of the holography program.

Table 3: List of Target, Reference, and Absent Antennas: X = Out, R = Reference

Date	1	2	3	4	5	6	7	8	9	10	11	12	13	14	15	16	17	18	19	20	21	22	23	24	25	26	27	28
14 Oct 11				R						R								R	X									
21 Oct 11				R						R								R	X							X		
22 Oct 11		R						X											X			R				R		
29 Oct 11	R			R				R			R							R	X								R	
30 Oct 11		R	R		R														X							R		R
07 Nov 11	R							R											X							R		R
28 Apr 12		X	X	X			R	X	X	R					X		R		R	X		X	R	X		R		R
29 Apr 12	R	X	X	X	R			X	X		R	R			X	R		R	R			X	X		R		X	X
21 Dec 14	R	R	X	R		R		R		R	R				R	R		R	R			R	R					
24 Dec 14			X			R		R		R		R	R						X		R				R	R	R	
28 Dec 14	R	R	X	R		R		R		R	R				R	R		R	X			R	R		R			
29 Dec 14	R	R	X	R		R		R		R	R				R	R		R	X			R	R		R			
31 Dec 14	R	R	X	R		R		R		R	R				R	R		R	R			R	R		R			
01 Jan 15			X		R		R		R			R	R	R							R			R		R	R	R
02 Jan 15			X		R		R		R			R	R	R							R			R		R	R	R
03 Jan 15	R	R	X	R		R		R		R	R				R	R		R			R	R		R		R		R
07 Jan 15	R	R	X	R		R		R		R	R				R	R		R			R	R		R		R		R
17 Jan 15					R		R	X		R		R	R	R						X	R		R		R		R	
20 Feb 15	R			X		R		R				X		R					X	R		R		R		R		R
27 Mar 16		R					R						R								R	R		R				R
16 Mar 17		R					R		R	R	R	X	R						R			R	R		R		R	R
22 Mar 17		R					R		R	R	R	X	R						R			R	R		R		R	R
29 Mar 17		R					R	X		R	R	R	X						R			R	R		R		X	R
10+16Apr17		R					R		R	R	R		X						R			R	R		R			R
11+12May17	R			R	X	R		R				R		R	R			R				R				R		R
20 Jan 19	R		R		R	R	X		R			R		R	R			R			R			R			R	X
21 Jan 19		R		R			X	R		R	R	R						R			R	R		R			R	X
18 May 20		R	R				R	R		R		R			R				X			R			R		R	R
27 May 20					R	R				R		R			R				X		R	R		R		R		R

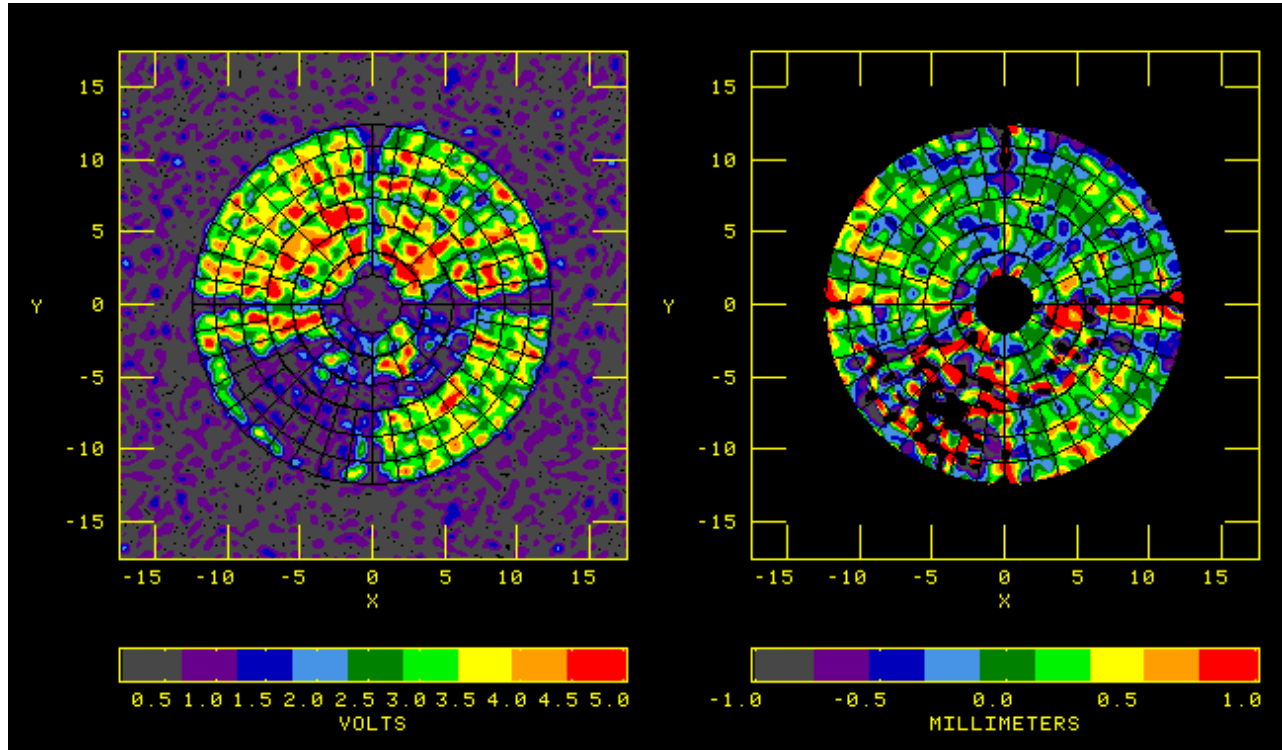


Figure 12: The apparent E-field amplitude (left), and surface panel deformation (right) for ea13 on 03 January 2015. The ‘missing’ panels are covered in snow, which has absorbed the signal from the calibrator source.

7.1 Improvement Example

As noted above, ea20’s surface had never been adjusted using high frequency observations. It was then no surprise that the new observations showed its surface shape was the worst of any antenna. Shown in Figure 13 is the improvement in the panel setting before and after the panels were set in early May, 2017. The left image is from a 49x49 raster taken on 10 and 16 April, 2017, while the right image was taken shortly afterwards, on 11 and 12 May, 2017. The

improvement is dramatic. The unweighted pre-fit rms is 0.59 mm prior to surface adjustment, and 0.29 mm after. Subsequent observations, made in 2018 and 2019 show no further changes.

Notable also is that this adjustment was done in the field – it is not necessary to make these panel adjustments with the antenna in the service barn.

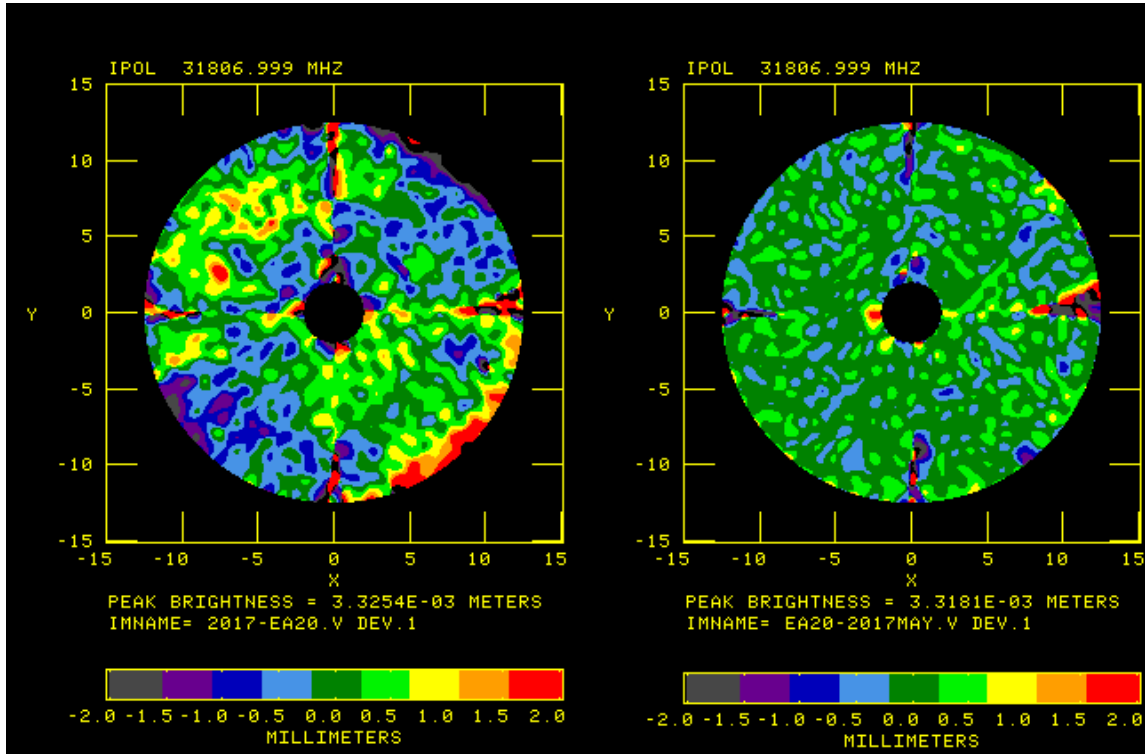


Figure 13: Showing the improvement in the surface accuracy of ea20. Data for the left image taken in April, 2017, and in May 2017 for the right image, following panel adjustments.

Six antennas have undergone panel adjustments since 2016 – ea01, ea04, ea15, ea17, ea20 and ea26. All have shown marked improvement in their surface following the adjustments. Five of the six are the best antennas in the array. The exception, ea01, has special issues, to be described later. Two more antennas (ea02 and 25) are scheduled for panel adjustments this year.

7.2 Panel Displacement Stability

The stability of the antenna surface over time is of critical importance. The process of holographic adjustment is quite costly – both in terms of time taken for the observations, and of the effort in physically resetting the panels. Proof that the changes made are valid for years is needed justify the effort expended.

Observations taken over many years show that the antenna surfaces are extremely stable over time. In Fig 14 is shown the surface displacements of ea14 at 33 GHz over five years – 2016 in the upper left, 2017 in the upper right, 2019 in the lower left, and 2020 in the lower right. All significant features (excluding those under the quad legs, where the SNR is very low) are faithfully reproduced. The rms deviations are the same in each – 0.35 mm, while the scatter in the difference between any two is 0.08 mm. The story is the same on all antennas.

The temperature of the antennas might be expected to have an effect on the panel accuracy, as any differential expansion between the panels and the supporting backup structure might cause vertical displacements of the central regions of each panel with respect to the edges. Two high-quality Q-band observations allow measurement of this effect. These were taken in the morning of 29 October 2011, and the early evening of 30 October, 2011. Although the timing of these two observations was not ideal (best would have been late at night, and in the afternoon), the ‘daytime’ observation was of 3C273, which in October is quite close to the sun. Hence this observation was taken with the antennas pointed within about 20 degrees from the sun, while the ‘night’ observation was entirely after sunset. The average panel difference image (‘day’ - ‘night’) for eight antennas is shown in Fig 14.

The figure clearly shows the centers of the panels are higher in the daytime than nighttime. The azimuthal supporting backup structures are clearly evident in the image, but there is little evidence for the radial supports having an effect

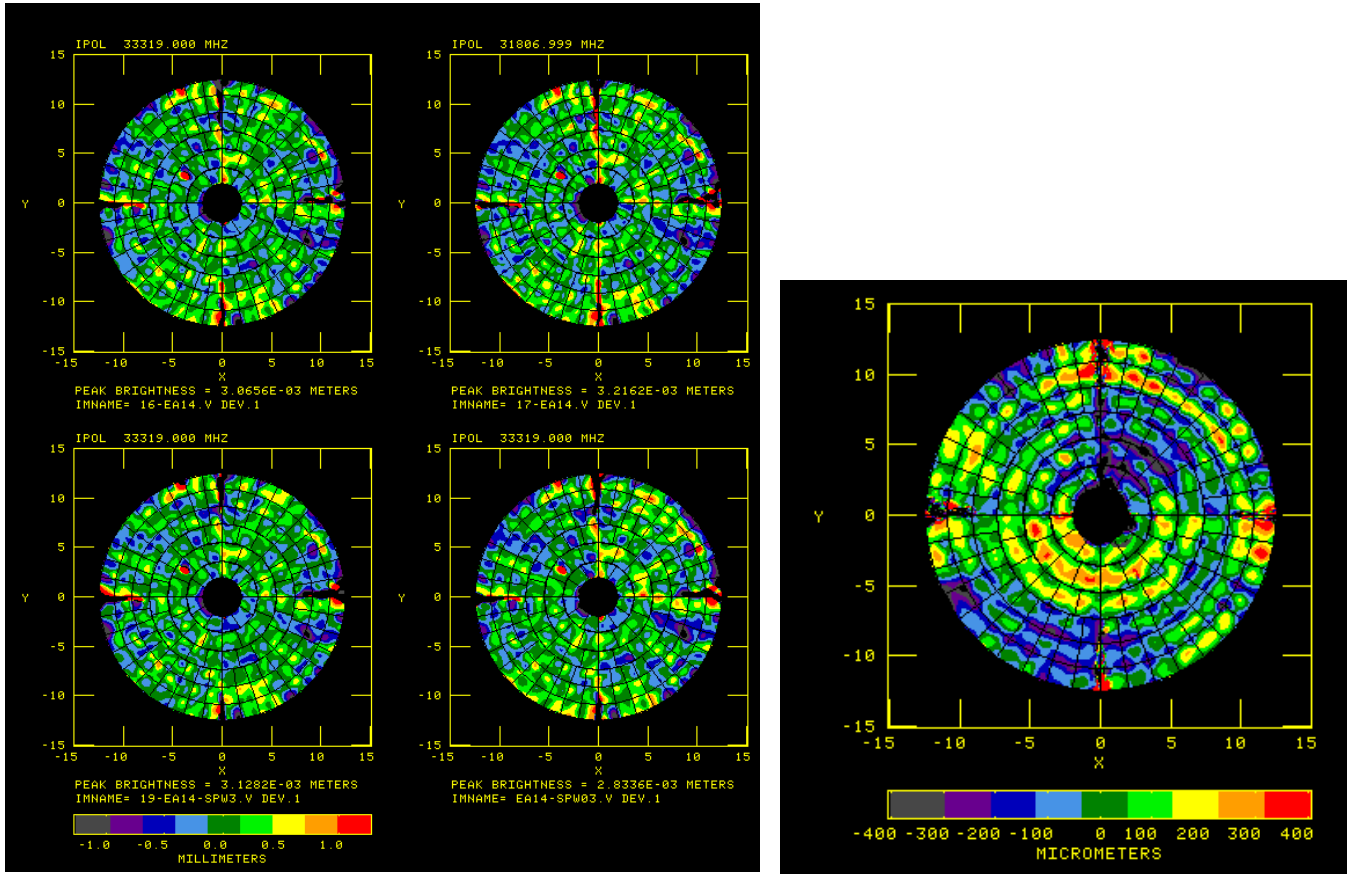


Figure 14: Panel Stability Plots: **(Left)** Showing surface stability for ea14 over a four-year period. The top two show surface displacements from observations taken in March 2016 and May 2017. The bottom two from observations in January 2019 and May 2020. The surface rms in each is 0.35mm (a typical value amongst antennas adjusted in the 1990s). The rms in the difference between any two images is 0.08 mm. **Right** The difference in panel setting, at 42 GHz, between a ‘daytime’ observation, with the antennas pointed to within 20 degrees of the sun, and a ‘nighttime’ observation, taken after sundown, one day later. The image is the average of eight antennas.

on the panel displacements. The typical differential center displacement is ~ 0.25 mm. The rms in the panel difference is about 0.12 mm, which we can interpret as the threshold for setting panels. Adjustments finer than this are smaller than than the typical night-day variations due to differential heating and expansion of the antenna primary surface.

Also visible in the image is a large-scale ‘cubic’ warp, seen most clearly at a position angle about -30 degrees from the vertical. The origin of this large-scale effect is uncertain, but might be connected to the large elevation range over which the data were taken – particularly for the ‘night’ observation, which spanned a range of 38 to 72 degrees. Gravity-induced warps will change most rapidly at high elevations.

7.3 Band Dependent Effects

Although the benefits of surface panel adjustments are clear – a more than doubling of the sensitivity of Q-band observations – there remain some issues which have so far defied easy explanation. The most puzzling are the band-dependent illumination amplitudes.

Data from all five high frequency bands for ea13 are shown in the following two figures. All are taken with the same physical resolution. Figure 15 shows the aperture illuminations at the five bands. All have been normalized such that the integral over the surface is 1.0. Note that the illumination becomes increasingly non-uniform as frequency increases¹⁰. There is little agreement in the illumination maxima and minima between frequency bands. Note that these differences cannot be due to the feed horns, nor is likely they are due to the subreflector, as the physical scales of perturbations

¹⁰Panel holography at lower frequencies has not been attempted. However, 101 x 101 raster observations at L-band, taken for a different purpose, show the illumination amplitude to be completely smooth over the aperture

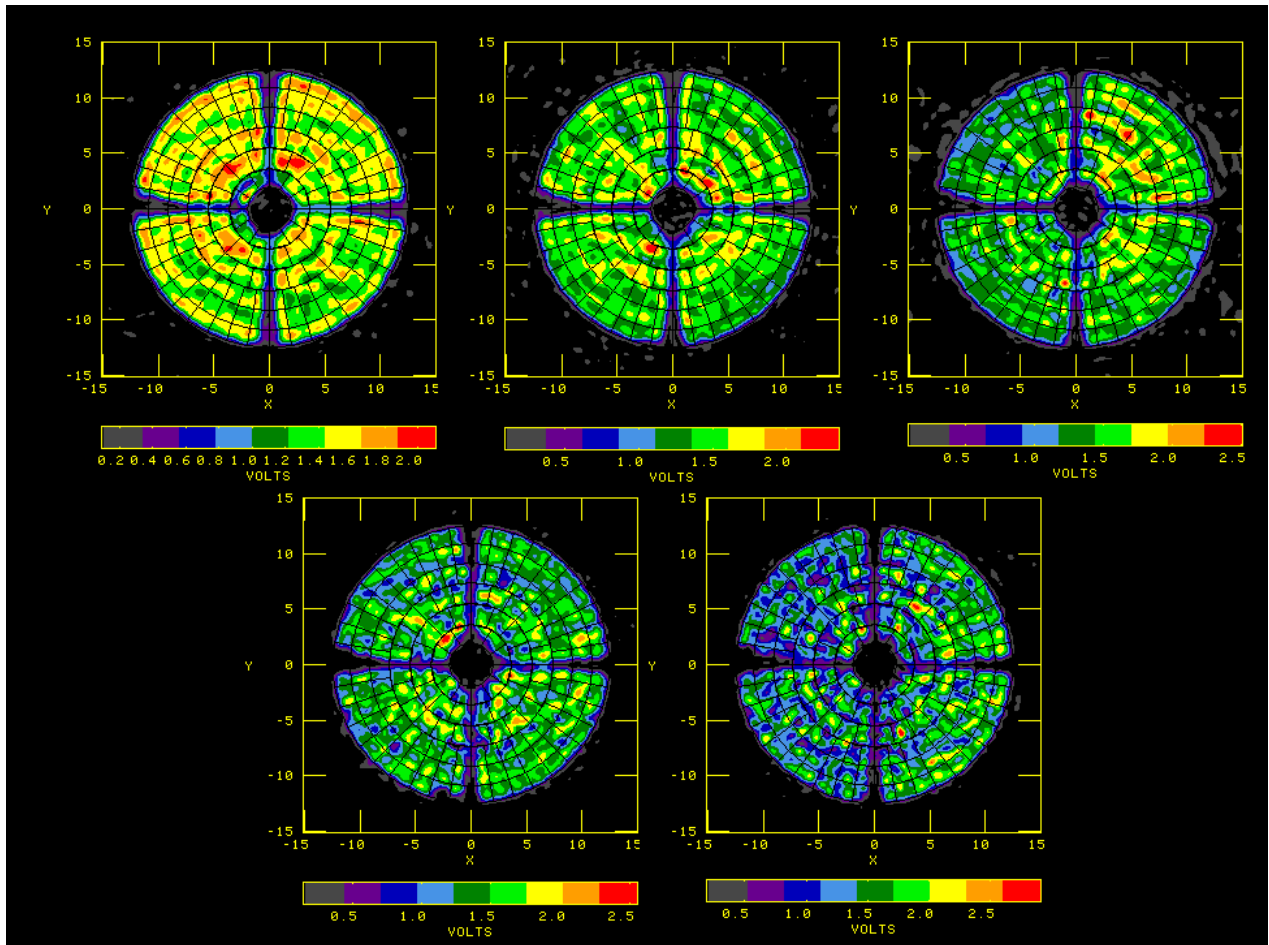


Figure 15: Antenna illumination amplitudes on ea13 for: X-band (upper left), Ku-band (upper middle), K-band (upper right), Ka-band (lower left), and Q-band (lower right). The higher the frequency, the ‘choppier’ the illumination amplitudes become.

caused by these optical elements is much larger than that seen in the images. The trend of increasingly ‘noisy’ panel amplitudes with increasing frequency is seen on all antennas.

In figure 16 I show the reflector panel deformations in ea13 for each of the five bands. Notable are the generally higher deviations with lower frequency, the apparent raised outer panels for X-band, and the ‘potato chip’ deformation most notable at Ku-band. These characteristics are generally seen at all bands. These large-scale perturbations cannot be due to the primary reflector, but could be due to the feed horn or the subreflector. However, if the latter, the ‘potato-chip’ shape should be seen with increased amplitude in the higher frequency images. This is not seen. However, note that this antenna had its surface adjusted using Q-band observations, so any imprint of the subreflector would have been removed from high frequency observations, as the K and Ka band horns straddle the Q-band horn.

A likely explanation for the increased ‘choppiness’ of the higher illumination amplitudes at high frequencies is that we are seeing horizontally unresolved sub-millimeter undulations on scales of tens of centimeters in the antenna panels themselves. If this is the case, the panel undulations would be resolved with high-resolution holography if the resolution is smaller than the putative irregularities. When resolved out, the observed amplitude fluctuations seen at lower resolution will disappear, to be replaced by larger irregularities in the panel phase corrections. It is unlikely the hypothesis can be tested however, as this requires an holography of at least 101 x 101, which would require more than 30 hours observing time in prime weather conditions¹¹.

¹¹But I’d love to try...

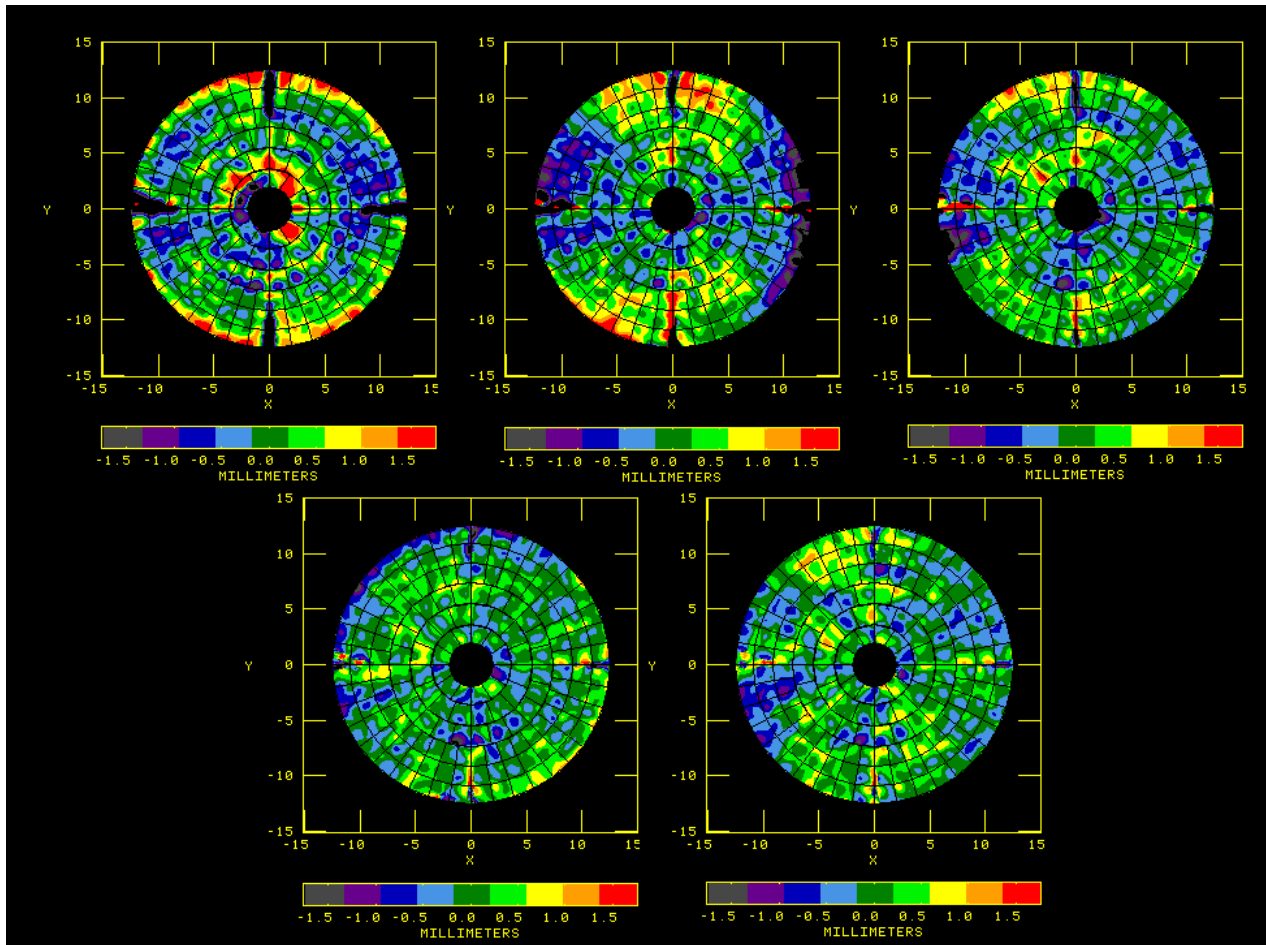


Figure 16: Antenna surface deviations for: X-band (upper left), Ku-band (upper middle), K-band (upper right), Ka-band (lower left), and Q-band (lower right).

7.4 Elevation Effects

Beam cuts made as part of the subreflector alignment project (reported on in EVLA Memo 211) clearly show the vertical profiles developing a large coma lobe and asymmetrical beam shape with decreasing elevation. The primary cause – a sag of the subreflector position – is neatly offset by counter-rotation of the subreflector. Although this operation largely removes the large coma lobe associated with the subreflector sag, it cannot offset an associated problem – gravitational warping of the main reflector when pointing to low elevations. As of this writing, we are still unsure of the magnitude of this effect. A new low-resolution holography program, utilizing 21 x 21 rasters at Ka-band has been defined to study the deformation of the antenna surfaces as a function of elevation. The results of this study will be published when ready.

8 Ranked List of Panel Modifications

The most recent dish panel observations were taken in May 2020. Given the demonstrated stability of the antenna surfaces, there is no need to repeat antenna holography, except perhaps as a check on the effects of subsequent surface adjustments.

Table 4 contains a ranked list of antennas, from worst to best. The ‘Pre’ and ‘Post’ values are the amplitude-weighted surface rms in millimeters. The former is the current surface, the latter is the estimated rms after full adjustments. The five best antennas have all had secondary panel adjustments (since 2017), and show a surface rms of typically 0.25 mm. The 12 worst antennas have rms deviations of 0.40 mm or more (up to 0.53 mm for ea05). Adjustments of these are recommended, with an estimated improvement in gain of 2 – 3 dB ($\sim 25\%$) at Q-band.

Table 4: Ranked List of Surface Accuracies

Rank	Ant	Pre	Post												
1	04	.24	.17	8	14	.35	.17	15	9	.39	.19	22	2	.44	.19
2	17	.25	.18	9	16	.36	.19	16	10	.40	.18	23	18	.44	.19
3	26	.28	.21	10	7	.37	.18	17	11	.40	.18	24	24	.44	.19
4	20	.29	.17	11	12	.37	.20	18	28	.40	.18	25	1	.45	.20
5	15	.30	.19	12	3	.38	.20	19	8	.41	.20	26	21	.45	.23
6	13	.30	.17	13	19	.38	.18	20	23	.41	.19	27	25	.45	.17
7	22	.33	.17	14	6	.39	.21	21	27	.43	.17	28	5	.53	.24

8.1 Can We Do Better?

The distribution of achieved rms surface accuracy suggests that an rms of about 0.25 mm represents the limiting level – the errors are likely dominated by irregularities within the panels themselves (which cannot be addressed through our four-corner mountings) and by errors in the panel adjustments. We know the latter is partly responsible, as, to date, corrections are only implemented if the absolute value of the correction exceeds 0.38 mm. The current best rms of about 0.25mm is compatible with the current panel setting limit. Hence, the current limiting value may be due to our failure to implement corrections below the current 0.38mm threshold.

The PANEL program used to generate the corner adjustments outputs the predicted rms should all corners be adjusted. As seen in Table 4, the predicted benefit of doing this is to reduce the overall surface rms to 0.15 to 0.2 mm. Although not a great improvement over the current levels, there should be a significant improvement in forward gain if a level of 0.15 mm could be achieved.

An expected improvement in gain through reduction of the surface irregularities can be obtained through application of Ruze’s formula for gain loss due to a gaussian distribution of panel irregularities:

$$G = \exp^{-(4\pi\sigma/\lambda)^2} \quad (38)$$

where σ is the surface rms. At $\lambda = 6$ mm, our shortest operating wavelength, a surface rms of 0.4 mm (typical for the worst antennas) leads to a loss of 50%, while at our current best of 0.25 mm, a loss of 25% is predicted. If we could achieve a panel rms of 0.15mm, a loss of just 10% would result. At this level, high-frequency observing is certainly limited by other factors, notably the gain loss due to elevation-induced deformations, and pointing irregularities not adequately removed by referenced pointing.

It should also be noted that we should not take the predictions from Ruze’s expression too strongly. Experience suggests it overpredicts the gain loss, likely because the distribution of panel errors is not gaussian. The only way to find out if implementation of all 688 screw adjustments is useful is by doing this on one antenna, preceded and followed by a careful measurement of antenna gain and sensitivity.

9 Two Odd Antennas

Two of our antennas have special issues. Here I briefly describe the problems.

9.1 Antenna 01

The problems with this antenna are described at length in Memo #211. Upon installation of the Q-band receiver on this antenna in the late 1990s, it was found that the subreflector had to be moved as far to the left as was physically possible (as seen from behind) in order to better balance the sidelobes and improve the forward gain. However, doing this made the sidelobes at lower bands more asymmetric. It seems the location of the Q-band feed is significantly offset from the correct location. It also appears that all the feeds on this antenna are significantly offset from their correct positions, but in different ways for each band – this situation complicates any simple correction. In an attempt to improve the Q-band performance, we have imposed a slight tilt to the subreflector, to permit positioning it closer to the center of the allowed motion. The result of this was to considerably improve the beam symmetry at Ku and K bands, but to notably worsen it at Ka-band, without significant improvement at Q-band.

The panel adjustments that were made in April 2020 used data taken in 2019 – before the subreflector adjustments were made. In Fig 17 is shown the surface image before and after these adjustments, using data taken in January 2019, and May 2020. Note that the ‘after’ image includes the effect of the subreflector tilt and shift. The error near the left edge of the dish is larger than a half-wavelength, so is seen as ‘black’ in the image, where it should be bright red. A lower-frequency holography run may be necessary to properly unwrap the ambiguity.

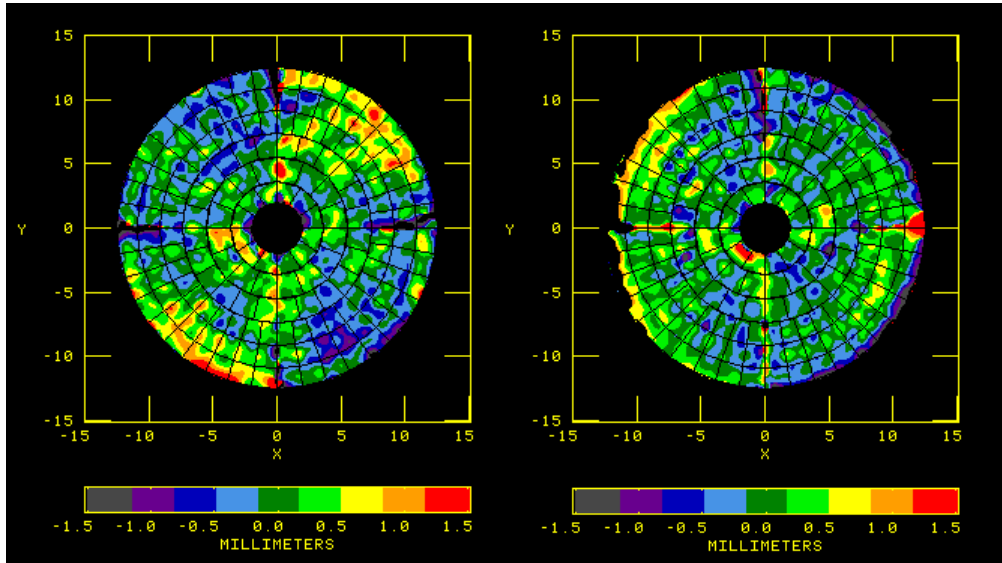


Figure 17: The antenna panel displacements in 2019 (left) and in 2020 (right) for antenna 01 following both the panel adjustments, and modifications to the subreflector tilt and offset. The astigmatic warp, and most small-scale irregularities visible in the left panel have been removed, but the subreflector changes have introduced strong phase errors near the left and right edges. The error is large enough to induce a phase ambiguity, visible as the abrupt transition from red to black on the left side of the antenna.

9.2 Antenna 21

All the holography images taken since 2014 show what appears to be missing panels in the upper part of ea21. Figure 18 shows the effect. Note the apparent absence of the two panels in the outermost ring, just to the right of the vertical quad leg. We are quite certain the panels are not missing! The rapid gradient in panel setting seen in the right panel of the figure hints at the origin – these two panels are tilted at an angle sufficient to generate a phase gradient large enough to decorrelate the amplitudes within the 80cm resolution beam. This is the second antenna to show such an effect – early in the holography program, one other antenna (ea18, if memory serves) was found to have a similar problem. Inspection of that antenna indicated that, during the original construction, the final two panels to be installed during construction were found to overlap. The ‘fix’ at that time was to depress (or raise) both until the edges lined up – thus generating the tilt. A similar effect is likely the cause of the ‘gaps’ in the illumination of ea21.

10 A Rogue’s Gallery

For completeness, we show the panel images for all 28 antennas. These are taken from the May 2020 observations, except for ea19 and ea01, which show data from earlier observations. The color wedge is the same on each, -1.0 to 1.0 mm. while antennas 21 through 28 are shown in Fig 19. Antennas ea01 through ea20 are shown in fig 20.

11 Acknowledgements

The work described here is the result of much effort by many individuals over the course of the nearly 30 years since the holography program began. Special thanks go to Mike Kesteven, who defined and implemented all the procedures still in use today, Ken Sowinski, for many discussion on the problems of antenna optics and for implementing the software changes to the on-line system, Eric Griesen, for converting the standalone code written by Mike and myself into the AIPS system, Michiel Brentjens, who wrote and implemented the code now used to properly sample the antenna beams for all offsets, and to Bob Broilo and Mike Romero, for their efforts in organizing the panel setting programs needed to implement the changes.

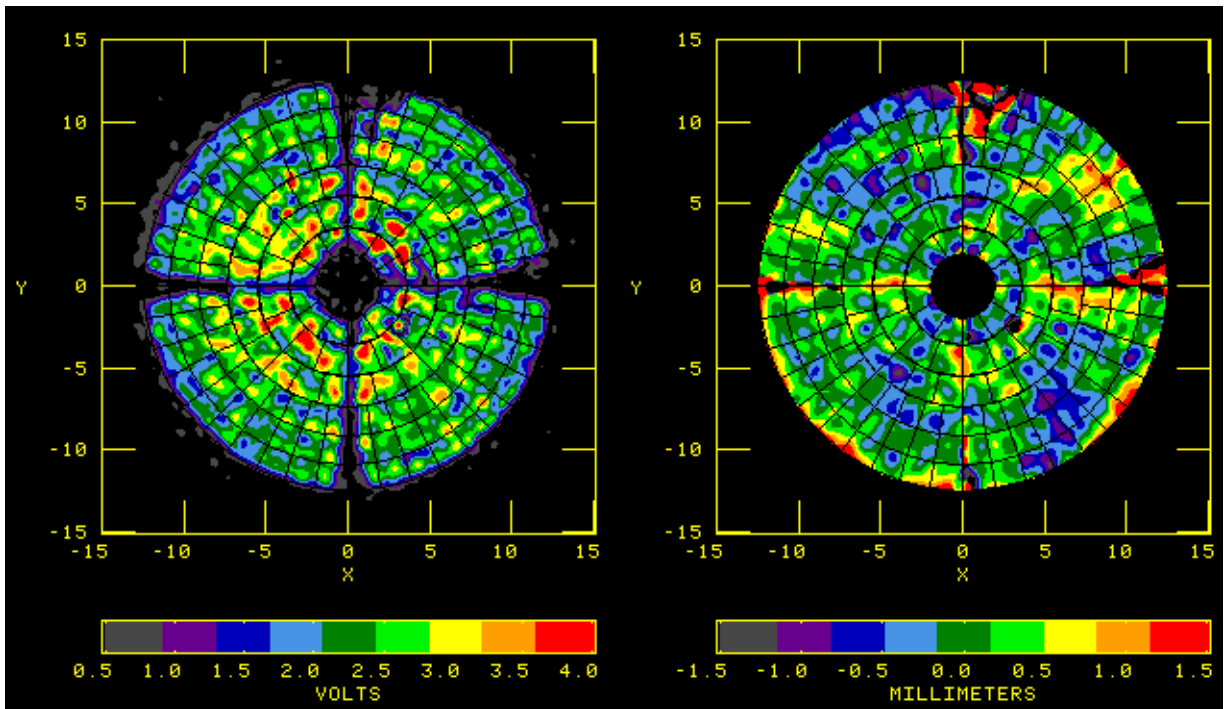


Figure 18: The amplitude (left) and panel displacement (right) images for ea21. Note the apparent missing panels in the outermost ring at the top of the antenna – the panels are there, but give no signal. They are evidently tilted sufficiently to generate a strong phase gradient, which decorrelates the signal over the resolution element of about 80cm.

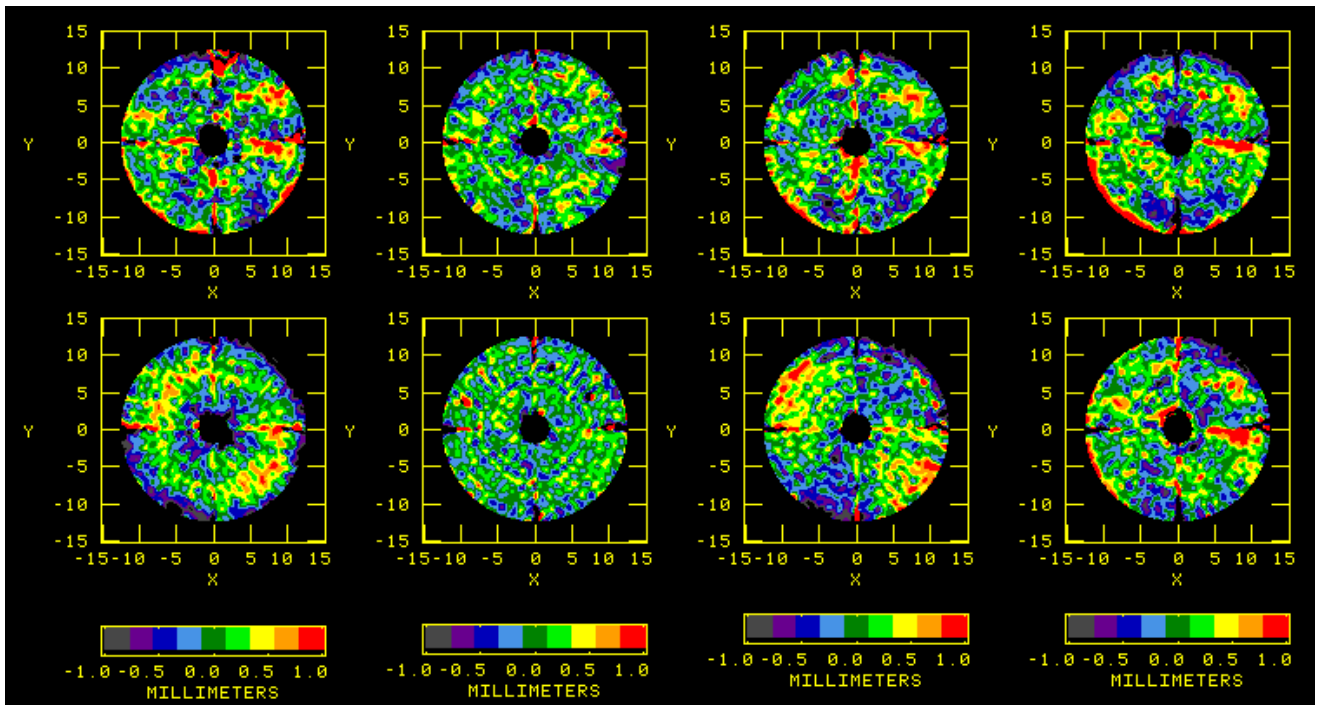


Figure 19: The panel displacements for antennas 21 through 28.

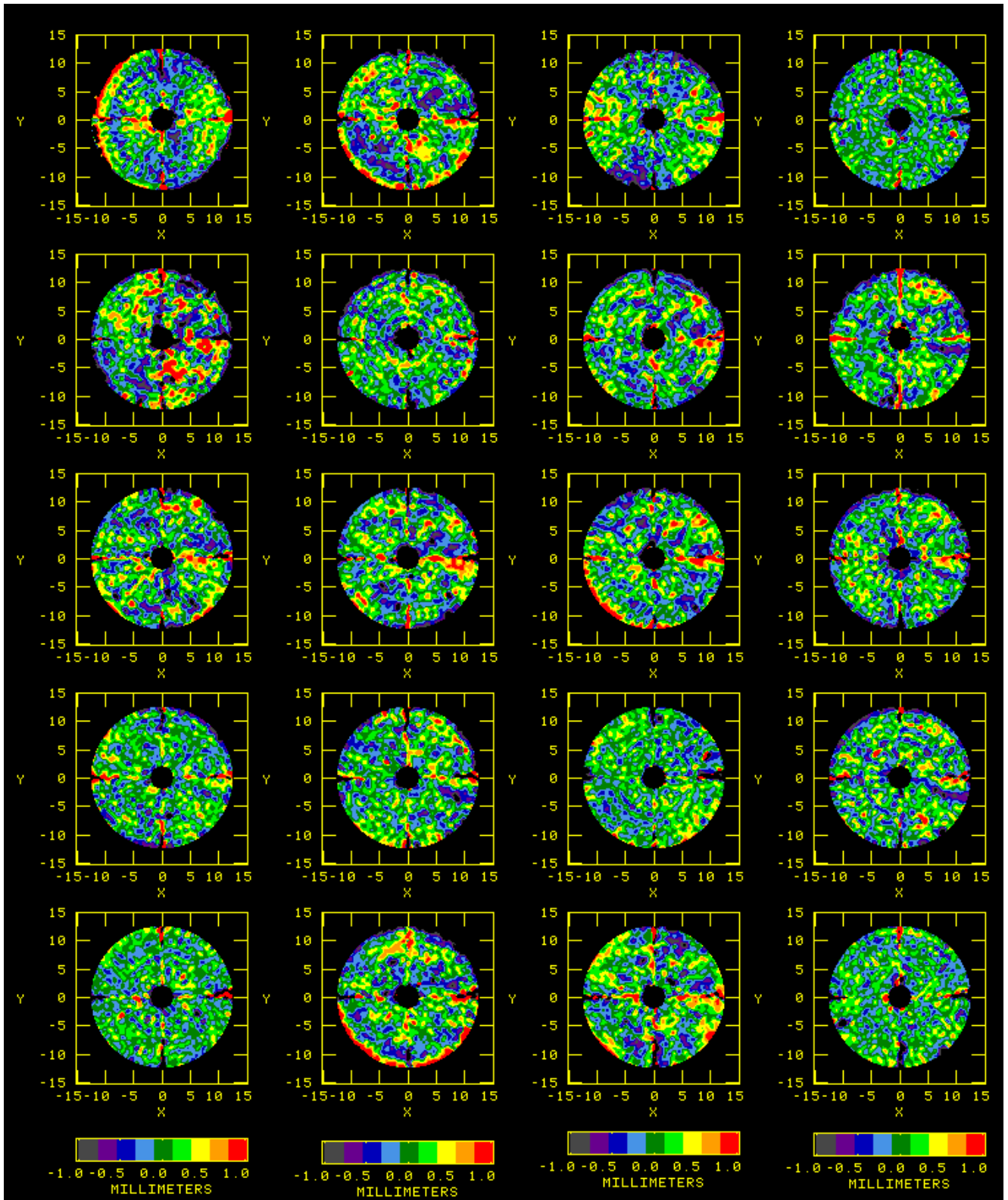


Figure 20: The panel displacements for antennas 1 through 20 (upper left to lower right). All images are made from Ka-band data taken in May 2020, except for ea01 and 19, which use earlier data.